Tampere University

Roman Kovalchukov

EFFECTS OF 3D DEPLOYMENTS ON INTERFERENCE AND SINR IN 5G NEW RADIO SYSTEMS

Faculty of Information Technology and Communication Sciences
Master of Science Thesis
November 2019

ABSTRACT

Roman Kovalchukov: Effects of 3D Deployments on Interference and SINR in 5G New Radio Systems
Master of Science Thesis
Tampere University
Communication Systems and Networks
Supervisors: Dr. Dmitri Moltchanov and Prof. Yevgeni Koucheryavy
Examiners: Dr. Dmitri Moltchanov and Prof. Yevgeni Koucheryavy
November 2019

Lately, the extremely high frequency (EHF) band has become one of the factors enabling fifth-generation (5G) mobile cellular technologies. By offering large bandwidth, New Radio (NR) systems operating in the lower part of EHF band, called millimeter waves (mmWave), may satisfy the extreme requirements of future 5G networks in terms of both data transfer rate and latency at the air interface.

The use of highly directional antennas in prospective mmWave-based NR communications systems raises an important question: are conventional two-dimensional (2D) cellular network modeling techniques suitable for 5G NR systems? To address this question, we introduced a novel, three-dimensional framework for evaluating the performance of emerging mmWave band wireless networks. The proposed framework explicitly takes into account the blockage effects of propagating mmWave radiation, the vertical and planar directivities at transceiver antennas, and the randomness of user equipment (UE), base station (BS), and blocker heights. The model allows for different levels of accuracy, encompassing a number of models with different levels of computational complexity as special cases. Although the main metric of interest in this thesis is the signal-to-interference-plus-noise ratio (SINR), the model can be extended to obtain the Shannon rate of the channel under investigation.

The proposed model was numerically evaluated in different deployment cases and communication scenarios with a wide range of system parameters. We found that randomness of UE and BS heights and vertical directionality of the mmWave antennas are essential for accurate evaluation of system performance. We also showed that the results of traditional 2D models are too optimistic and greatly overestimate the actual SINR. In contrast, fixed-height models that ignore the impact of height on the probability of exposure to interference are too pessimistic. Furthermore, we evaluated the models that provide the best trade-off between computational complexity and accuracy in specific scenarios and provided recommendations regarding their use for practical assessment of mmWave-based NR systems.

Keywords: 5G mobile communication, blockage, directive antennas, interference, millimetre wave communication, millimetre wave antenna arrays, numerical analysis, radio links, SIR, SINR, stochastic geometry, stochastic processes, three-dimensional modeling

PREFACE

The results of this research were presented at the IEEE Global Communications Conference (GLOBECOM) [1] and published in two scientific journals [2, 3].

I would like to express my genuine gratitude to my supervisors, Dr. Dmitri Moltchanov and Prof. Yevgeni Koucheryavy, for setting the tasks and providing guidance, advice, and assistance at all stages of the thesis. Also, I sincerely thank all my friends and colleagues from Tampere University for their support, help, and contributions to my personal growth. In particular, I want to thank Asst. Prof. Sergey Andreev, Dr. Aleksandr Ometov, and Andrey Samuylov for their fruitful cooperation and willingness to share their experiences.

Finally, I would like to thank my friends and family for being patient and supportive during my studies and research.

Tampere, Finland, 20th November 2019

Roman Kovalchukov

CONTENTS

LIST OF FIGURES

LIST OF TABLES

LIST OF SYMBOLS AND ABBREVIATIONS

$1/\mu_R$	Mean height of Rx
$1/\mu_T$	Mean height of Rx
$1/\mu_B$	Mean communication entity's height
A	Factor accounting for Tx power and gains
$\alpha_{R,H}$	Planar Rx antenna directivities
$\alpha_{R,V}$	Vertical Rx antenna directivities
$\alpha_{T,H}$	Planar Tx antenna directivities
$\alpha_{T,V}$	Vertical Tx antenna directivities
χ	Spherical angle for wavefront density
d_I	Distances from tagged Rx to the interfering Tx
d_T	Distances from tagged Rx to the tagged Tx
$E[I_1^n]$	Single source interference moments
$E_n(x)$	Exponential integral function
$f_X(x)$	RV X probability density function
$f_{\vec{X}}(\vec{x})$	RVs $\vec{X}$ joint probability density function of
$\{\gamma, \theta, \beta\}$	Angles defining vertical exposure probability
$\Gamma(z)$	Euler Gamma function
G_r	Distance from LoS to blockers top
H_B	Blocker's body height
H_{IR}	Heights of interfering Rx
H_{IT}	Heights of interfering Tx
H_R	Rx height
H_T	Tx height
H_n^z	Struve function
I	Aggregate interference
$\mathbb{J}$	Jacobian of transformation
J_n^z	Bessel function of the first kind
$K_{P_R,I}$	Covariance between interference/received power
λ	Spatial density of Rx nodes

λ_B	Spatial density of blockers
$L_P(r)$	Path loss at distance
L_x	Horizontal spherical geodesic
L_y	Vertical spherical geodesic
μ_I	Mean of interference
μ_{P_R}	Mean received power
N	Number of interferers
$p_B(r)$	Blockage probability at distance r
$p_C(d)$	Exposure probability
$p_H(d)$	Planar exposure probability
P_R	Received power
P_T	Transmited power
$p_V(d)$	Vertical exposure probability
r_B	Blocker's body radius
ρ	Spherical excess of a rectangle
R_I	Radius of an area around the tagged Rx, from where interference can be received
R_i	i-th Rx
R_T	Maximum distance between tagged pair of devices
S	Signal-to-interference ratio
S_A	Surface area of a wavefront
σ_I^2	Variance of interference
T_i	i-th Tx
x_i	i-th element of vector $\vec{x}^n$, $i = 1, 2, \ldots, n$
ξ_i, η_i	Auxiliary variables
$\vec{x}^n$	Variables vector of size n
ζ	Path loss exponent
3GPP	The 3rd Generation Partnership Project
4G	fourth generation of broadband cellular network technology
5G	fifth generation of broadband cellular network technology
AP	Access Point
BS	Base Station
CDF	Cumulative Distribution Function
D2D	Device-to-Device

DVB	Digital Video Broadcasting
eMBB	Enhanced Mobile Broadband
GSM	Global System for Mobile Communications
GSMA	GSM Association
IMT	International Mobile Telecommunication
IoT	Internet of Things
jpdf	Joint Probability Distribution Function
LoS	Line-Of-Sight
LT	Laplace Transform
LTE	Long Term Evolution
MEF	Metro Ethernet Forum
METIS	Mobile and wireless communications Enablers for the Twenty-twenty Information Society
MIMO	Multiple-Input and Multiple-Output
mMTC	Massive Machine-Type Communications
mmWave	Millimeter-wave band of radio frequency spectrum between 30 GHz and 300 GHz
MulteFire	LTE-based technology that operates standalone in unlicensed and shared spectrum, including the global 5 GHz band
NGMN	Next Generation Mobile Networks Alliance
NR	New Radio
OFDM	Orthogonal Frequency-Division Multiplexing
ONF	Open Networking Foundation
pdf	Probability Distribution Function
PPP	Poisson Point Process
QoS	Quality of Service
RV	Random Variable
Rx	Receiver
SINR	Signal-to-Interference-plus-Noise Ratio
SNR	Signal-to-Noise Ratio
Tx	Transmitter
UAV	Unmanned Aerial Vehicle
UE	User Equipment
URLLC	Ultra-Reliable Low-Latency Communications

1 INTRODUCTION

Thanks to the introduction of advanced communication technologies in future fifth-generation networks (5G) [4], it will be possible for a typical user to carry up to several mobile and wearable devices [5]. These high-performance wearable devices can communicate with each other while nearby using millimeter-wave radio frequency (mmWave) technology in ultra-dense networks. Using mmWave technology provides significantly higher throughput and lower latency with comparison to the conventional cellular radio technologies at frequencies up to 60 GHz [6]. According to the experts' opinions, mmWave systems will be a key enabler of 5G mobile cellular networks, allowing supporting connections that are comparable with wired networks in terms of channel capacity via extremely wide frequency bandwidths and spatial frequency reuse technology.

In this regard, recently, the attention of researchers has been attracted by the use of mmWave frequency bands, such as 28, 60, and 72 GHz [7]. Stronger mmWave signal propagation attenuation is partially mitigated by the possibility of the use of strongly directional antennas on both sides of the wireless link. The scientific community expects the usage of antennas with high directionality to lead to a decrease in interference and, consequently, to an increase in performance under a so-called noise limited regime [8]. Also, mmWave frequency electromagnetic waves are unable to penetrate objects greater in size than a few centimeters. Therefore, physical bodies on the way of radio wave propagation path, for example, cars, humans, trees, are blockers for the propagation of electromagnetic waves at these frequencies [9].

The ever-increasing intricacy of the wireless communication scenarios accompanies the evolution of cellular networks in the 5G era under consideration. The alleged use of unmanned aerial vehicles (UAV) to provide communication services to large crowds of people, in conjunction with the pervasive use of high-performance wearable devices (for example, augmented reality glasses), requires the study of wireless communication channels in three dimensions [10]. Similarly, emerging superdense 5G deployments [11], encompass another concept of device-to-device (D2D) communications that are supposed to expand the capabilities of 5G wireless networks significantly. These scenarios also require study in all three dimensions as the heights of interacting objects may vary drastically.

1.1 Significance of 3D Models

As a rule, earlier, the performance of cellular communication systems was predicted using two-dimensional stochastic geometry tools [12]. These models represent communication entities by the implementation of a 2D stochastic process. The reason why this approach is so popular is the small transmitters and receivers antennas directivities and assumption of constant heights of communicating devices. Multiple times researchers showed [13] that under such assumptions, stochastic geometry methods reflect well enough key performance indicators, including interference, signal-to-interference ratio (SIR), and channel capacity.

The new tendency to use higher frequency ranges in which wider bandwidths are available for 5G systems reopens the discussion about the need for three-dimensional models. Researchers [14] describe in detail the mathematical model describing the work of 3D Massive MIMO technology, which takes into account the change in antenna height, which allows improving signal-to-interference plus noise ratio (SINR) systems. Also, in [15], a more realistic case of 3D+ was considered. Authors in [16] describe the approach of using three-dimensional fluid models, allowing estimation of the SINR cumulative distribution function (CDF). Researchers have shown that their proposed model shows better results than a two-dimensional model.

1.2 Stochastic Geometry Models for Evaluating the SIR in 3D

Despite the broader use of antennas with narrower beam angles, random heights of interacting objects, and the occurrence of the line of sight (LoS) blocking, two-dimensional stochastic geometry tools prevail in the arsenal of researchers for analyzing the efficiency of mmWave networks. Interference and SIR random variables (RVs) moments for scenarios utilizing extremely high frequencies in the presence of blockages were obtained in [17, 18]. The interference Laplace transform (LT) and the SIR probability density functions (pdf) without considering blockage effects were obtained in [19], and SIR LTs for a millimeter-wave system operating at a frequency of 28 GHz in [20, 21]. In [22], the authors analyzed the SIR effects of atmospheric absorption on system performance of mmWave and terahertz models. However, all of the mentioned studies suggest two-dimensional flat scenarios, which can introduce a substantial miscalculation of the interference effects in millimeter-wave systems, which naturally affects the estimation of SIR and received power.

Lately, several authors have challenged the simplified two-dimensional approximations of cellular networks, which in reality, are three-dimensional. A study in [23] showed that approximations using only two dimensions, traditionally used in planning wireless networks, with a few illustrative examples, lead to significant divergence from the optimal solution. It is noteworthy that the conclusion was that network deployers, algorithm developers, and policymakers utilize a small set of path loss models, often under the assumption

of constant antenna heights for the receivers. In this connection, the quality of the results of network planning can be significantly affected by the use of approximation by a two-dimensional model. From the above, we can conclude that more complex three-dimensional models are required. In particular, the authors, in some scenarios, identified deviations of SINR reaching 20 dB. Similar results were also presented in [24, 25].

The main goal of this work was to develop a three-dimensional stochastic geometry framework for evaluating SINR. The model takes into account the features of wireless networks operating in the millimeter frequency range, such as the directivity of antennas, the effect of signal blockages by human bodies, and random heights of communication entities. Additional interest is to compare the effectiveness of various special cases of models in terms of accuracy and computational complexity.

2 MILLIMETER WAVE 5G NEW RADIO SYSTEMS

The goal of the 5G communication networks is to satisfy the ever-increasing mobile communication needs of states, enterprises, and also individual citizens [4]. It is assumed that 5G networks will play a key role in turning cities into smart cities, which will allow citizens and society as a whole to receive the socio-economic benefits that an advanced digital economy with intensive use of data provides [26]. The concept of building 5G communication networks promises to improve the quality of service for end-users by offering new applications and services with gigabit data transfer speed, as well as significantly increasing the performance and reliability of the communication services. 5G networks will be built on the successes of previous-generation mobile networks that have transformed society by providing new services and business models. In particular, 5G networks will enable wireless operators not only to provide communication services but also to develop their new solutions and services for consumers and industry in various sectors.

5G commercial networks are expected to begin rolling out after 2020 when standardization of such systems will be completed. The GSM Association (GSMA) expects the number of simultaneous connections to 5G networks to reach 1.1 billion by 2025, which will be about 12 percent of the total number of connections [27]. It is also projected that total operator revenue will grow by an average of 2.5 percent, reaching $ 1.3 trillion by 2025 [28].

2.1 5G Systems and Services

On the technical side, it is expected that 5G networks will significantly increase the data transfer rate and reduce the delay compared to previous generation networks. In particular, 5G communication networks are designed to provide a delay of less than 1 ms on a wireless access site, which is a prerequisite for mission-critical services which implies that data is highly sensitive to delivery time. High-speed access at the subscriber site, reaching 10 Gbit/s, will allow 5G networks to provide a wide range of high-throughput broadband access technologies and will change the conventional approach to the “last mile” segment.

5G communication networks will support various data rates provided to users, covering various usage scenarios [29, 30]. Following the requirements for 5G systems defined in Recommendation ITU-R M.2083 [31], see Fig. 2.1, the total peak data transfer rate of 5G is expected to reach 10 Gb/s. However, under certain conditions and scenarios, it should

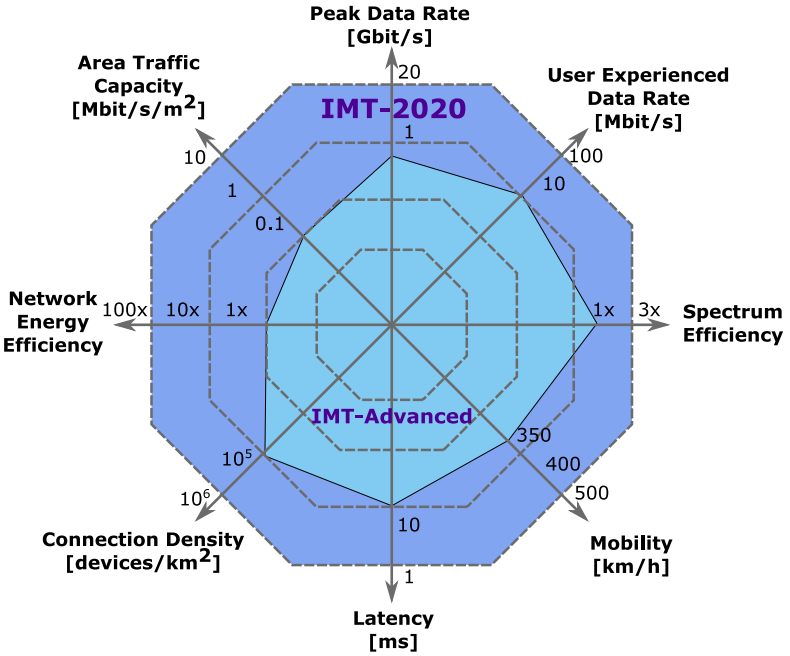

Figure 2.1. *Requirements for 5G networks*

support a peak data rate of up to 20 Gb/s. For large areas deployments, for example, in urban and suburban spaces, it is expected that the data transfer rate for the user should be 100 Mb/s. In areas with extreme requirements, the data transfer rate per user should reach higher values, for example, up to 1 Gbit/s indoors.

It is expected that the spectrum utilization efficiency in 5G communication networks will be two to three times higher compared to 4G [31]. It is also assumed that 5G communication networks will provide spatial capacity reaching 10 Mbit/s/m^2 in areas with high requirements, for example, areas, shopping centers. The energy consumption for a 5G radio access network should not be higher than that of 4G networks deployed today. Therefore, at the development stage, the energy efficiency of both base stations (BS) and user equipment (UE) should be increased at least to the same extent as the expected increase in 5G bandwidth compared to 4G. In addition to the specified requirements, 5G networks in particular regimes should grant a delay on the wireless interface of no more than 1 ms, thus providing support for services with extremely high latency requirements. Also, 5G communication networks should provide support for subscribers with high mobility, whose speed reaches 500 km/h while maintaining the required quality of service (QoS) parameters. Such services are to be provided, in particular, in high-speed trains. Finally, 5G communication networks will need to maintain a subscriber density of up to 106/km^2, for example, in ultra-dense scenarios of inter-machine communication.

2.1.1 5G Networks Standardization Process

Several international organizations are developing 5g communication network standards. Among them, there are several official organizations involved in specifications prepa-

ration for the system as a whole, as well as specialized industry alliances with narrow specialization in particular areas.

The 3rd Generation Partnership Project (3GPP) is in charge for defining and supporting the standards of current and future generations of mobile communications technologies. The 3GPP consortium consists of the following groups: (i) Radio Access Network, (ii) Service and Systems Aspects, (iii) Core Network and Terminals. Each of them also includes several working groups. 3GPP uses a parallel “Releases” approach and establish standards by outlining three stages that are incremental towards defining a range of services, network architecture, and finally, detailed specifications of system interfaces.

The European Telecommunications Standardization Institute (ETSI) conducts standardization activities that define the requirements, functionality, and building blocks for the entire 5G system. Several technical committees actively collaborate with 3GPP and, in some cases, solve the tasks identified by 3GPP.

ITU is coordinating the development of global telecommunication standards in addition to stimulating growth and sustainable development of the sector and ensuring universal access to current system specifications. ITU activities focus on three main sectors. (i) The telecommunications sector (ITU-T) defines global telecommunication standards. (ii) The radiocommunication sector (ITU-R) regulates the global radio frequency spectrum. (iii) The development sector (ITU-D) supports the ITU mission to ensure equitable, sustainable communication technologies. Within ITU, there is International Mobile Telecommunication 2020 (IMT-2020 standard), which is a set or requirements for systems and their components that support advanced features beyond the scope of IMT-2000 (3G) and IMT-Advanced (4G). IMT-2020 has the following objectives: (i) to coordinate the 5G network research process, (ii) to determine the structure and long-term targets of the 5G evolution, (iii) to develop a plan according to which the standardization process should be completed by 2020.

Industrial alliances affect the standardization of 5G communication networks by representing the interests of specific industry groups, as well as large international projects. The groups presented in the reports include, in particular, the following alliances and projects 5G-PPP, DVB, ONF, MulteFire, MEF, NGMN, METIS.

2.1.2 Set of 5G Services

Communication service providers, equipment manufacturers, together with organizations involved in standardization of 5G communication networks, have identified several potential uses for such networks [29, 32, 33]. Based on the analysis, organizations standardized for three fundamentally different categories of services:

- Enhanced Mobile Broadband (eMBB);
- Ultra-Reliable Low-Latency Communications (URLLC);
- Massive Machine-Type Communications (mMTC).

The eMBB service aims at meeting the needs of ultrahigh-speed user applications at the subscriber access site [34]. Applications requiring such speeds include viewing the augmented and virtual reality glasses and helmets, big data access, high-resolution video transferring. eMBB is expected to be the primary use case for 5G in its early deployments [35]. eMBB will also allow consumers to use high-speed on-demand streaming services for the home screens, and mobile devices and will provide further development of corporate services. Some operators see eMBB as the solution to the “last mile” in areas where there are no optical access networks [36, 37].

Low latency and high security of 5G communication systems will be one of the main goals pursued by the development of intelligent transport systems of the future, allowing vehicles to communicate with each other, creating new opportunities for the introduction of autonomous cars and trucks [38]. For example, an autonomous vehicle operated through a cloud-based driving system must be able immediately to stop, accelerate, or turn, according to the instructions received [39]. Any delay in transmitting information on the network or signal loss from the base station that impedes message delivery can lead to catastrophic consequences. The low latency makes 5G networks also suitable for remote surgery, production automation, and real-time process control [40, 41, 42].

5G communication networks are also expected to contribute to the planing of smart cities and the Internet of Things (IoT) by deploying sensor systems in cities and rural areas [43, 44, 45].

2.2 NR Radio Interface

New Radio is going to be a key enabler of 5G to deliver different types of services, from low-speed mMTC to ultra-high capacity requirement eMBB and URLLC services. 5G communication networks provide access to several frequency bands at once. For example, applications with low latency and short-range (suitable for densely populated urban areas) will use the millimeter frequency range (above 24 GHz). When more coverage is required, and access speed is not the main factor, service providers will use radio frequencies below 1 GHz. While lower frequencies have better propagation characteristics and, as a result, are characterized by better coverage, higher frequencies provide greater capacities due to wider bandwidth ranges.

Key technological components to achieve these goals include a flexible physical layer frame structure, a network access method with delay optimization, the use of antenna arrays, and flexible interaction between access networks operating in the high-frequency and low-frequency spectrum [98].

Like LTE, the NR radio access network is based on the Orthogonal Frequency-Division Multiplexing (OFDM) method with the possibility of precoding with discrete Fourier transform to increase the gain in the transmission direction [99; 100]. NR maintains a flexible wireless interface structure with subcarrier spacing in the range from 15 kHz to 240 kHz and corresponding cyclic prefix, providing single technology to support various deploy-

ments, from small cells with high capacity in mmWave frequency range to large cells with a carrier frequency of less than 1 GHz. The low spacing of the subcarriers allows the use of a longer cyclic prefix. Whereas the NR physical layer structure is independent of the frequency band, not all supported wireless interface structures are applicable for all NR frequency bands. For the 0.45-6 GHz frequency band, the available subcarrier separation is 15 MHz, 30 MHz, and 60 kHz, while the maximum channel size corresponding to these subcarriers is 50 MHz, 100 MHz, and 200 MHz. The minimum and maximum channel sizes for the 24 - 72 GHz frequency band are 100 MHz, 200 MHz, and 400 MHz, which allows the use of carrier spacing of 60 kHz and 120 kHz for the implementation of 3300 subcarriers. Providers can use carrier aggregation function In cases where it is necessary to maintain even higher bandwidth.

NR also allows adapting the channel bandwidth on the UE side to reduce device power consumption. Therefore, NR defines the so-called Bandwidth Parts (BP), which indicates the frequency band in which the UE is currently operating. If a UE is capable of simultaneously receiving multiple BPs, it is, in principle, permissible to mix transmissions of different frame structures for one UE. Note that version 15 of the 3GPP standard defines support for only one BP per receiver. Work in the millimeter frequency range is another example of the efficient use of mini-slots, since the available bandwidth is substantial, since only a few OFDM symbols may be enough to complete the transmission.

2.3 Specifics of Millimeter Waves

Currently, the millimeter-wave spectrum is only starting to be used by cellular communication systems [46]. The reason is the specific features of the propagation of radio waves, including high losses of propagation, atmospheric and water absorption, higher scattering due to increased effective roughness of materials, significant losses upon penetration through objects, low diffraction and, besides, due to strong phase noise and high equipment costs. However, many of these disadvantages can be effectively resolved, allowing the use of a new spectrum of frequencies for radio access networks. Authors in [47] have made a comprehensive study of these effects, some of those will be summarized bellow.

2.3.1 Propagation Loss

According to the standard Friis propagation model, an increase in the carrier frequency leads to a significant growth of propagation losses [48]. However, at the same physical aperture size, the transmitting and receiving antennas at greater frequencies emit and collect more energy using thinner radiation patterns [49]. In practice, it is possible to maintain the same effective aperture of the antenna using antenna arrays by forming a radiation pattern.

The impact of the number of antenna elements on the NR BS on the signal to noise ratio (SNR) as a function of distance is illustrated in Fig. 2.2 for radiated power $P_T = 23$ dBm,

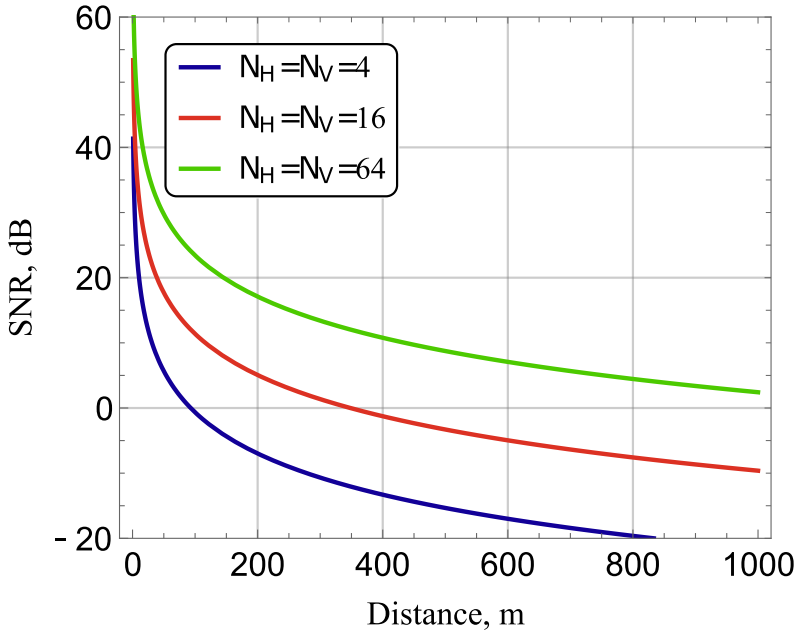

Figure 2.2. *SIR as function of number of antenna elements*

Table 2.1. *Weather effects*

Type	Density	Measurements
Rain, [54, 55, 56]	50 mm/h	10 GHz: 3 dB/km, >10 GHz: 10 dB/km
Fog, [57, 58]	0.5 g/m^3	50.44 GHz: 0.16 dB/km
Snow, [59]	700 g/m^3	35−135 GHz: 0.2-1 dB/km
Foliage, [60, 61]	0.5m^2/m^3	28.8 GHz: 1.7 dB/m, 73 GHz: 0.4 dB/m

where NV and NH are the number of antenna elements in the horizontal and vertical planes, respectively. Note that the use of antenna arrays also allows increasing the potential service area of one NR BS significantly. Today, there are practical implementations of antenna arrays in which the number of elements exceeds 512 [50, 51, 52].

2.3.2 Weather Effect

Measurements of the influence of weather conditions on the propagation of millimeter waves are fairly well studied [53], see Table 2.1. Note that foliage has the most significant effect when the signal drop reaches 2 dB/m. Losses caused by heavy snow, fog, and clouds are quite negligible (less than 1 dB/km). Rain is usually characterized by an additional attenuation of about 10 dB/km, which can seriously affect the characteristics of the communication channel. The influence of weather conditions on the SNR is illustrated in Fig. 2.3 for radiated power P_T =23 dBm and a different number of antenna elements on an NR BS. Note that the use of antenna arrays allows overcoming the negative impact of weather conditions.

2.3.3 Atmospheric Absorption

Additional losses in the propagation of millimeter-wave radio waves are introduced by absorption in the atmosphere [62, 63]. The main components responsible for the absorption in the frequency range under consideration are oxygen and water vapor. The absorption graph is shown in Fig. 2.4. Of particular note is the absorption of oxygen, which reaches 15 dB/km at a frequency of 60 GHz [64]. However, in general, absorption is not significant both for indoor communications and for prospective deployments in urban cellular networks, where the distance between the BSs is about 200 meters. In this case, absorption is advantageous since it allows one to reduce interference from neighboring BSs.

2.3.4 Dynamic Blockage

Since millimeter waves are characterized by lower diffraction, the line of sight blocking between the BS and the UE leads to much more significant losses compared to access networks operating at frequencies below 6 GHz [65, 66]. In particular, dynamic blocking introduces additional losses of the order of 15−40 dB [67, 68]. The duration of blocking depends on the density of dynamic blockers [69]. It should be noted that in the presence of an LoS blockage, the use of reflected signal propagation paths may not provide the best propagation conditions. Thus, reflection from rough surfaces, such as concrete or brick, can attenuate millimeter-wave signals by 40−80 dB [70].

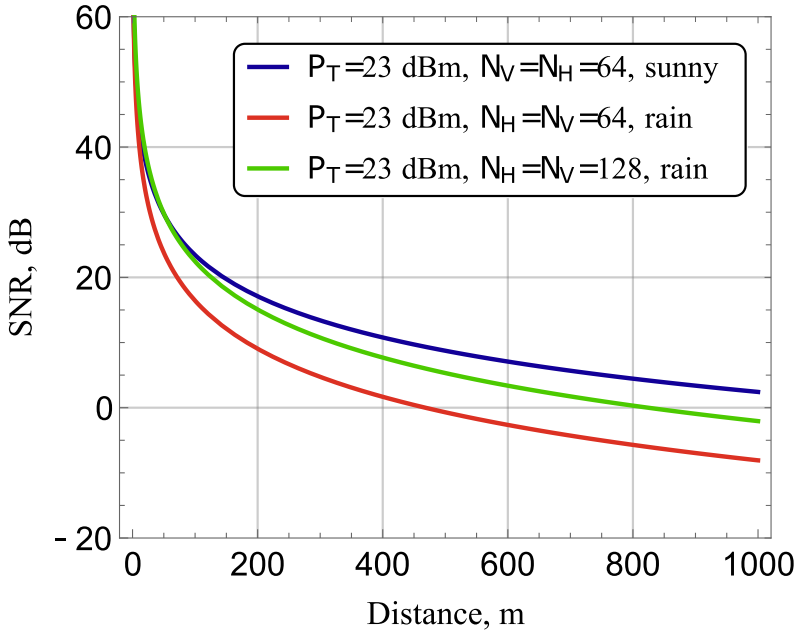

Figure 2.3. *SNR as a function of distance and weather conditions*

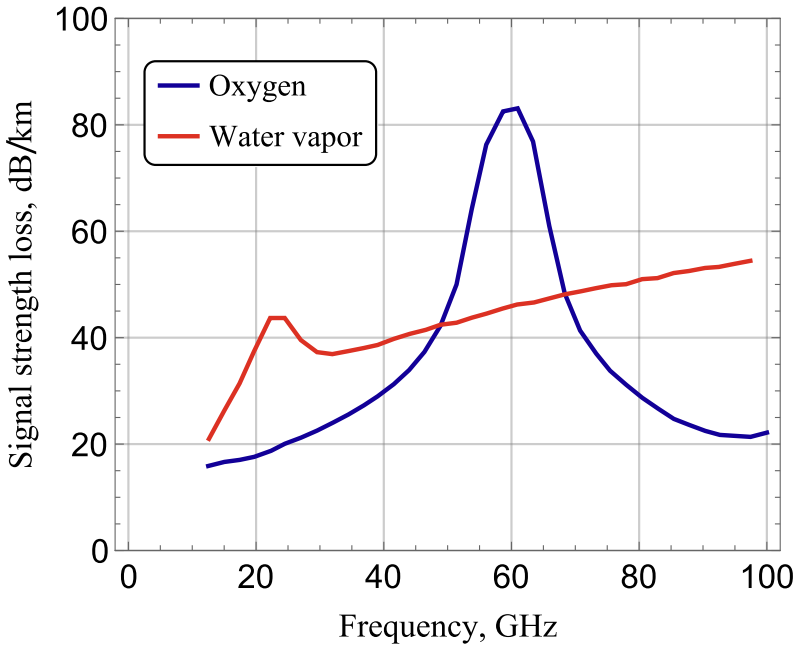

Figure 2.4. *Millimeter-wave energy absorption in the atmosphere*

3 3D MMWAVE NR MODELING: INTERFERENCE AND SIR

In [1] we studied mmWave scenarios with high and omni directional antennas on the Tx and Rx in the communication link, respectively. We showed that for specific ranges of the parameters the difference between two- and three-dimensional models can be as high as 40 dB for the SIR values. This drastic differences cannot be neglected as they can lead to drastic mistakes on the stage of deployment planing of mmWave networks.

3.1 Stochastic Geometry Signal-to-Interference Ratio Model

In this section we formalize the stochastic geometry model for the mmWave communication scenarios with highly directional antennas taking into account random positions and heights of the communicating devices and mmWave specific propagation and blocking characteristics.

3.1.1 mmWave Network Model

First, we assume that all the communicating devices use the same frequency range, what implies the possibility of interference exposure from the neighboring transmitters, i.e. interferers. Fig. 3.1 demonstrates the considered model and main features and types of interacting devices. Projections of R_i, $i = 0, 1, \dots$ represent receivers' coordinates are assumed to follow Poisson point process (PPP) in $\Re^2$ with spatial intensity λ. Every receiver R_i has it's tagged communicating transmitter T_i. We assume that the transmitters position follows the uniform distribution inside the circle of radius R_T around it's tagged receiver. Tx and Rx heights, H_T and H_R, assumed to follow an exponential distribution where μ_T and μ_R are the distribution parameters. Txs and Rxs carriers bodies aremodeled as cylinders with exponentially distributed with parameter μ_B height, H_B, and constant radius r_B.

Let us chose a random tagged pair of communicating devices (R_0, T_0). Lets define a circle around R_0 with radius R_I and drop from the consideration all the interferers outside the circle, considering their effect insignificant, i.e., lower than the noise level. We calculate R_I based on the communication devices characteristics such as noise figure and other and signal propagation model. Fig. 3.1 depicts four types of Tx-Rx pairs, target transmission, pair of devices and antenna patterns are shown in green color, gray-colored

entities represent pairs that do not contribute to the total interference received by the target receiver due to miss-alignment of the antenna patterns. Blue pairs do not contribute to the interference due to blockage by the bodies in the scenario. Finally only red pair contributes to the total interference received by the target receiver.

We also assume that the bodies of the target pair may block the interfering signal. On top of that, additional PPP representing other bodies that can obstruct the propagation of the signal (e.g. random passers.)

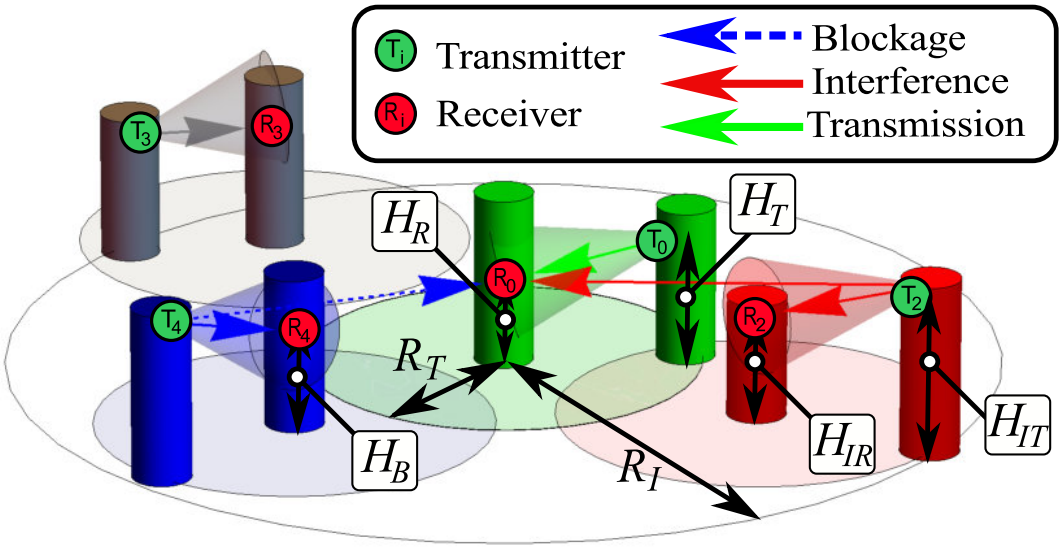

Figure 3.1. *Considered 3D communication scenario*

3.1.2 Signal Propagation and Antenna Patterns

For the calculating of the received power we use the following path loss model [71]

$$P_R(r) = Ar^{-\zeta}, \tag{3.1}$$

where A is the parameter that sums up Tx and Rx antenna gains, losses (except propagation loss), central frequency and transmitter power, r is the euclidean distance from transmitter to receiver, and ζ is the path loss exponent. Assuming the same type but with different number of vertical and horizontal elements of the Tx and Rx antennas, the antenna pattern simplified to a pyramidal zone with vertical and horizontal HPBW angles, $\alpha_{T,V}$ and $\alpha_{T,H}$, respectively, as shown in Fig. 3.2. This abstraction implies a flat gain on the main lobe inside the angle and the zero gain of side and rear lobes of the antenna pattern.

In our study the path loss coefficient ζ is taken from [70].

To find the gain A as a function of angles (α_V, α_H), we utilize the fact that the wavefront surface area is a spherical rectangle, as shown in Fig. 3.2. $\cos\chi$ can be found by the

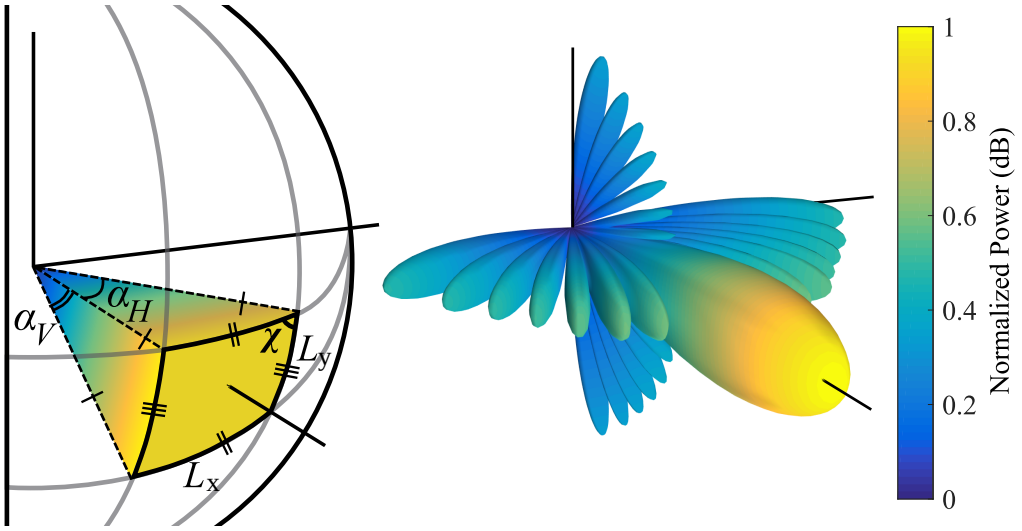

Figure 3.2. *Simplified and real antenna radiation pattern*

spherical law of cosines [72],

$$\cos\chi = \frac{\cos\left(\frac{\pi}{2}-\frac{L_x}{2}\right)-\cos\left(\frac{\pi}{2}-\frac{L_x}{2}\right)\cos\left(L_y\right)}{\sin\left(\frac{\pi}{2}-\frac{L_x}{2}\right)\sin\left(L_y\right)} = \frac{\sin\left(\frac{L_x}{2}\right)}{cos\left(\frac{L_x}{2}\right)}\frac{1-\cos\left(L_y\right)}{\sin\left(L_y\right)} = \\ = \tan\left(\frac{L_x}{2}\right)\tan\left(\frac{L_y}{2}\right). \tag{3.2}$$

From Fig. 3.2 we notice that a quarter of rectangle spherical excess equals to $(\rho - \pi/2)$, that implies

$$\cos\left(\rho-\frac{\pi}{2}\right) = \tan\left(\frac{L_x}{2}\right)\tan\left(\frac{L_y}{2}\right), \tag{3.3}$$

where L_x and L_y are spherical geodesic lines.

The spherical geodesics L_x and L_y are equal to the directivity angles α_H and α_V respectively at the unit distance from the center. Thus, the spherical rectangle area is equal to

$$S_A = 4\arcsin\left(\tan\frac{\alpha_V}{2}\tan\frac{\alpha_H}{2}\right). \tag{3.4}$$

Since the power density follows $P_R = Ar^{-\zeta}$, coefficient of the antenna gain which correspond to the angles α_V and α_H, are equal to

$$G(\alpha_V,\alpha_H) = \frac{4\pi}{S_A} = \frac{\pi}{\arcsin\left(\tan\frac{\alpha_V}{2}\tan\frac{\alpha_H}{2}\right)}, \tag{3.5}$$

which leads to $A = P_T G\left(\alpha_{T,V},\alpha_{T,H}\right) G\left(\alpha_{R,V},\alpha_{R,H}\right)$.

The final form of the expression of the received power at distance r is

$$P_R(r) = \frac{\left[\arcsin\left(\tan\frac{\alpha_{V,R}}{2}\tan\frac{\alpha_{H,R}}{2}\right)\right]^{-1}}{\arcsin\left(\tan\frac{\alpha_{V,T}}{2}\tan\frac{\alpha_{H,T}}{2}\right)} P_T\pi^2 r^{-\zeta}. \tag{3.6}$$

3.1.3 Investigated Network Performance Parameters

The main indicators of network performance that are of interest in this work are the mean of the aggregated interference and SIR, as ones of the central indicators, which characterizes the quality of the channel and affects many parameters of the wireless communication system performance.

The total interference mean is

$$I = A \sum_{i=1}^{N} d_i^{-\zeta}, \tag{3.7}$$

and SIR mean is

$$S = \frac{A d_0^{-\zeta}}{A \sum_{i=1}^{N} d_i^{-\zeta}} = \frac{d_0^{-\zeta}}{\sum_{i=1}^{N} d_i^{-\zeta}}, \tag{3.8}$$

where N - is a RV, which follows Poisson distribution with parameter equal to $\lambda \pi R_I^2$. d_0 and d_i, $i = 1, 2 \dots N$, are the euclidean distances in $\Re^3$ betwixt the target pair and tagged receiver and $i-$th interferer.

3.2 Model Analysis and Performance Indicators

In this section, we evaluate SIR in the presented three-dimensional scenario of a millimeter-wave wireless network. To begin with, we propose the average SIR approximation via the second-order Taylor series expansion. Later we introduce the main propositions and corollaries. Then, we study several special cases of the model.

3.2.1 Taylor Expansion for SIR

To evaluate the average SIR, we utilize SIR function $S = h(x, y) = P_R/I$ Taylor expansion. In particularly its the second-order approximation. We find it by expanding $h(x, y)$ near $\vec{\mu} = (E[P_R], E[I]) = (\mu_{P_R}, \mu_I)$, coming to [73]

$$E[h(\vec{\mu})] \approx h(\vec{\mu}) + \frac{h''_{xx}(\vec{\mu})\sigma^2_{P_R} + 2h''_{xy}K_{P_R,I} + h''_{yy}(\vec{\mu})\sigma^2_I}{2}, \tag{3.9}$$

where σ_I^2 is the variances of total interference I, $\sigma^2_{P_R}$ is the variance of received useful signal P_R, and $K_{P_R,I}$ is the covariance between two.

Noticing that

$$h''_{xx}(x, y) = 0,\ h''_{x,y}(x, y) = -y^{-2},\ h''_{yy}(x, y) = 2x/y^2, \tag{3.10}$$

we attain to the next approximation

$$E[P_R/I] \approx \frac{\mu_{P_R}}{\mu_I} - \frac{K_{P_R,I}}{\mu_I^2} + \frac{\sigma_I^2 \mu_{P_R}}{\mu_I^3}. \tag{3.11}$$

Using Campbell's theorem we get every central moment of aggregated interference [12]

$$E[I^n] = \int_0^{R_I} E[I_1^n(r)] p_C(r)[1 - p_B(r)] 2\lambda\pi r dr, \tag{3.12}$$

where, $p_C(r)$ is the exposure probability, $p_B(r)$ is the blockage of the LoS probability, and $E[I_1^n(r)]$ are the signal from a random interferer central moments at the distance r betwixt it and tagged receiver.

3.2.2 Main Propositions and Corollaries

Summarizing, to get the average SIR value, we first need to find: (a) average received power, $\mu_{P_R} = E[P_R]$, (b) first and second moments of interference from single source, $E[I_1^n]$, $n = 1, 2, \ldots$, (c) exposure probability, p_C, (d) blockage probability $p_B(r)$, conditioned on the distance r, and (e) the covariance between the useful received power and the interference power $K_{P_R,I}$.

Proposition 1. The moments of power of the received signal are equal to

$$E[P_R^n] = A^n 2^{\frac{1}{2}-\zeta n} \left[W\left(\mu_T, \mu_R\right) + W\left(\mu_R, \mu_T\right)\right] \times \frac{\pi^{\frac{3}{2}} \csc\left(\frac{\pi\zeta n}{2}\right) \sec\left(\frac{\pi\zeta n}{2}\right) R_T^{-\left(\frac{n\zeta-5}{2}\right)}}{\mu_R^2 \mu_T^2 \left(\mu_R + \mu_T\right) \Gamma\left(\frac{n\zeta}{2}\right) \Gamma\left(\frac{n\zeta-1}{2}\right)}, \tag{3.13}$$

where $W(x, y)$ has the form

$$W(x,y) = x^3 \Big[2\sqrt{2} y^{\zeta n} R_T^{\frac{n\zeta+1}{2}} + R_T^2 2^{\frac{\zeta n}{2}} y^{\frac{n\zeta+3}{2}} \Gamma\left(\frac{n\zeta-1}{2}\right) \times \\ \times \left(\cos\left(\frac{\pi\zeta n}{2}\right) H_{\frac{3-n\zeta}{2}}^{yR_T} - J_{\frac{n\zeta-3}{2}}^{yR_T} - \sin\left(\frac{\pi\zeta n}{2}\right) J_{\frac{3-n\zeta}{2}}^{yR_T} \right) \Big].$$

Proof. First we express the received signal power as

$$P_R = A \left(\sqrt{(H_T - H_R)^2 + r^2} \right)^{-\zeta}, \tag{3.14}$$

where H_T, H_R, and r are random variables.

Probability Density $|H_T - H_R|$ as the absolute value of the difference of two exponentially distributed RVs takes the form

$$f_{|H_T - H_R|}(y) = \frac{(e^{-y\mu_R} + e^{-y\mu_T})\mu_R\mu_T}{\mu_R + \mu_T},\ y > 0. \tag{3.15}$$

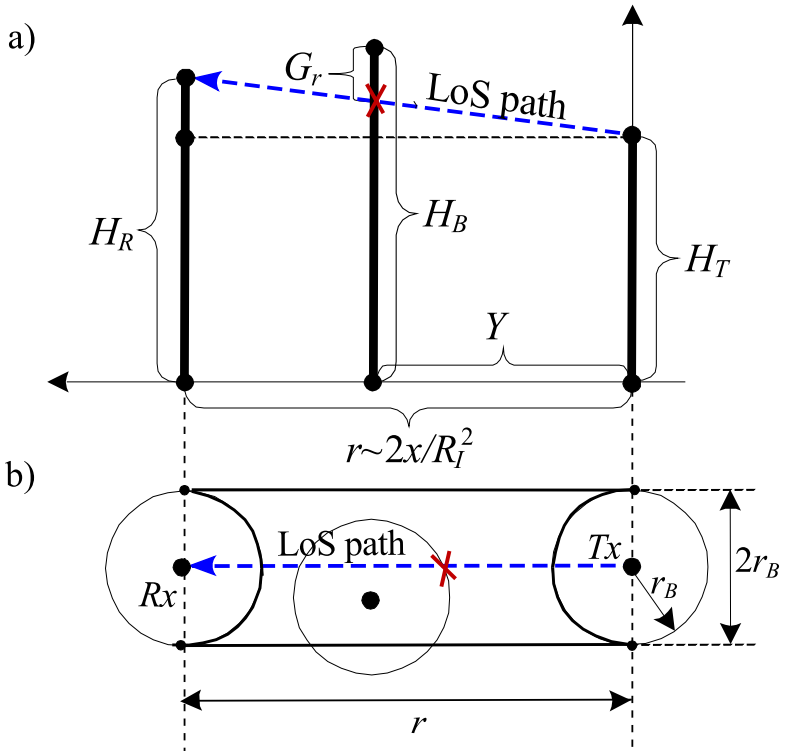

Figure 3.3. *LoS blockage Illustration*

Then the required received signal power moments $E[P_R^n(r)]$, $n = 1, 2, \ldots$, obtained following [74]

$$E[P_R^n] = \int_0^{R_T} \int_0^{\infty} \frac{A^n \left(e^{-y\mu_R} + e^{-y\mu_T}\right) \mu_R \mu_T 2r}{\left(r^2 + y^2\right)^{\frac{n\zeta}{2}} \left(\mu_R + \mu_T\right) R_T^2} dy dr. \tag{3.16}$$

Simplifing (3.16), we arrive at (3.13). □

Corollary 1. Interference moments can be obtained directly from (3.16), fixing the distance on the plane between the source of interference and the receiver, r, and take the form

$$E[I_1^n(r)] = \frac{\left[W_1(\mu_T) + W_1(\mu_R)\right] \left[\left(\mu_R + \mu_T\right) \Gamma\left(\frac{n\zeta}{2}\right)\right]}{2^{-\frac{n\zeta+1}{2}} A^n \pi^{\frac{3}{2}} \mu_R \mu_T}, \tag{3.17}$$

Where

$$W_1(x) = \left[\frac{r}{x}\right]^{\frac{1-n\zeta}{2}} \left[2J^{rx}_{\frac{n\zeta-1}{2}} \csc\left(n\pi\zeta\right) - J^{rx}_{\frac{1-n\zeta}{2}} \sec\left(\frac{n\pi\zeta}{2}\right) + \csc\left(\frac{n\pi\zeta}{2}\right) H^{rx}_{\frac{1-n\zeta}{2}}\right]. \tag{3.18}$$

Proposition 2. The blockage probability in the PPP of blockers with Txs and Rxs heights

which folows exponential distribution can be found as

$$p_B(r) = 1 - \left(\frac{\mu_R \mu_T}{(\mu_B + \mu_R)(\mu_B + \mu_T)} \right)^{\frac{2 r_B r \lambda \mu_R \mu_T}{\mu_B (\mu_B + \mu_R + \mu_T)}}. \tag{3.19}$$

Proof. To get LoS blockage likelihood we define the LoS blockage zone, which is illustrated in Fig. 3.3. Noticing that the LoS line will be obstructed only if a blocker befalls into this zone, we find the blockage probability $p_B(r)$ as follows.

Let G_r, $0 < r < R_I$, be the RV, representing the distance between the LoS and the height of the blocker HB at a 2D-distance r from the transmitter. Assuming $H_R \geq H_T$:

$$G_r = \frac{(H_R - H_T)Y}{r} + H_T - H_B, \tag{3.20}$$

where H_T, H_B, and H_R are random variables with a exponential distribution, Y is a RV evenly distributed over $(0, r)$. For the case when $H_R < H_T$, we need to re-substitute RV Y with $(r - Y)$. Yet, since Y follows uniform distribution over $(0, r)$, then $(r - Y)$ and Y are identically distributed RVs.

The likelihood that one blocker located at a distance r from Rx overlaps the LoS

$$p_{B,1}(r) = 1 - Pr\left\{ \frac{(H_R - H_T)Y}{r} + H_T - H_B > 0 \right\}. \tag{3.21}$$

Following the Poisson process properties, we get the probability blocking as follows

$$p_B(r) = 1 - \sum_{i=0}^{\infty} \frac{(2\lambda r_B r)^i}{i! e^{2\lambda r_B r}} [1 - p_{B,1}(r)]^i = 1 - e^{-2\lambda r_B r} - \sum_{i=1}^{\infty} \frac{(2\lambda r_B r)^i}{i! e^{2\lambda r_B r}} [1 - p_{B,1}(r)]^i, \tag{3.22}$$

here $p_{B,1}(r) = Pr\{G_r - H_B > 0\}$ is unknown.

Concede $\vec{\xi} = \{\xi_1, \xi_2, \xi_3, \xi_4\} = \{H_B, H_R, H_T, Y\}$ with joint probability distribution function (jpdf)

$$f_{\vec{\xi}}(\vec{x}) = \frac{\mu_B e^{-\mu_B x_1} \mu_R e^{-\mu_R x_2} \mu_T e^{-\mu_T x_3}}{r}, \tag{3.23}$$

and defining $\{\eta_1\} = \{G_r\}$ as the target variable. Adding auxiliary variables

$$\vec{\eta} = \{\eta_1, \eta_2, \eta_3, \eta_4\} = \{G_r, H_R, H_T, Y\}, \tag{3.24}$$

the transformation takes the form

$$y_1 = f(\vec{x}) = G_r = \frac{(x_2 - x_3)x_4}{r} + x_3 - x_1, \tag{3.25}$$

where the auxiliary functions are $f_i(\vec{x}) = x_i$, $i \in \{2, 3, 4\}$.

Noticing that the RVs transform is a one-to-one correspondence we come to

$$x_1 = \phi_1(\vec{y}) = -\frac{ry_1 - ry_3 - y_2y_4 + y_3y_4}{r},$$

which is complemented by $x_i = \phi_i(\vec{y}) = y_i$, $i \in \{2,3,4\}$.

Thereupon the sought jpdf is

$$f_{\vec{\eta}}(\vec{y}) = f_{\xi}(\phi_1(\vec{y}), \ldots, \phi_n(\vec{y}))|\mathbb{J}|, \tag{3.26}$$

where $f_{\vec{\xi}}(\phi_1(\vec{y}), \ldots, \phi_n(\vec{y}))$ can be set as

$$f_{\vec{\xi}}(\vec{\phi}(\vec{y})) = \frac{\mu_R\mu_T\mu_B}{r} \times e^{\frac{\mu_B(ry_1 - ry_3 - y_2y_4 + y_3y_4)}{r} - y_2\mu_R - y_3\mu_T}, \tag{3.27}$$

and the Jacobian of the transformation is equal to $\mathbb{J} = \partial\phi_1(\vec{y})/\partial y_1 = -1$.

pdf G_r can now be written as

$$\begin{aligned}
f_{\eta_1}(y_1) &= \iiint\limits_{\mathrm{R}^3} f_{\vec{\xi}^n}[\phi_i(\vec{y}^n)]|\mathbb{J}|dy_2dy_3dy_4 = \\
&= \int\limits_0^r \int\limits_0^\infty \int\limits_{l_1(\vec{y})}^\infty \frac{\mu_R\mu_T\mu_B}{r} e^{\frac{\mu_B(ry_1 - ry_3 - y_2y_4 + y_3y_4)}{r} - y_2\mu_R - y_3\mu_T} dy_2dy_3dy_4 = \\
&= \int\limits_0^r \int\limits_0^\infty \frac{\mu_R\mu_T\mu_B}{r\mu_R + \mu_By_4} e^{\frac{r\mu_By_1 - ry_3(\mu_T+\mu_B) + \mu_By_3y_4 - (r\mu_R + \mu_By_4)\max\left\{0, r(y_1-y_3)y_4^{-1} + y_3\right\}}{r}} dy_3dy_4 = \\
&= \int\limits_0^r f_{\eta_1\eta_4}(y_1, y_4)dy_4,
\end{aligned} \tag{3.28}$$

where

$$l_1(\vec{y}) = \max\left\{0, \frac{y_2y_3 - ry_2}{y_3}, \frac{-ry_2 + ry_4 + y_2y_3}{y_3}\right\}, \tag{3.29}$$

coming to the integrand

$$\begin{aligned}
&f_{\eta_1\eta_4}(y_1, y_4) = -\frac{(y_4\mu_B + r\mu_R)^{-1} e^{-\frac{ry_1\mu_R}{y_4} - \frac{ry_1\mu_T}{r-y_4}} \mu_B\mu_R\mu_T}{(r\mu_B - y_4\mu_B + r\mu_T)(-r\mu_R + y_4\mu_R + y_4\mu_T)} \times \\
&\times(-e^{\frac{ry_1\mu_T}{r-y_4}} ry_4\mu_B + e^{\frac{ry_1\mu_T}{r-y_4} + ry_1\left(\frac{\mu_R}{y_4} + \frac{\mu_T}{-r+y_4}\right)} ry_4\mu_B + e^{\frac{ry_1\mu_T}{r-y_4}} y_4^2\mu_B - \\
&- e^{\frac{ry_1\mu_T}{r-y_4} + ry_1\left(\frac{\mu_R}{y_4} + \frac{\mu_T}{-r+y_4}\right)} y_4^2\mu_B + e^{\frac{ry_1\mu_R}{y_4}} r^2\mu_R - e^{\frac{ry_1\mu_R}{y_4}} ry_4\mu_R - \\
&- e^{\frac{ry_1\mu_R}{y_4}} ry_4\mu_T - e^{\frac{ry_1\mu_T}{r-y_4}} ry_4\mu_T + e^{\frac{ry_1\mu_T}{r-y_4} + ry_1\left(\frac{\mu_R}{y_4} + \frac{\mu_T}{-r+y_4}\right)} ry_4\mu_T).
\end{aligned} \tag{3.30}$$

Changing the integration order, we get

$$p_{B,1}(r) = 1 - \int\limits_0^r \int\limits_0^\infty f_{\eta_1\eta_4}(y_1, y_4)dy_1dy_4 = \frac{\mu_R\mu_T \log\left(\frac{\mu_R\mu_T}{(\mu_B+\mu_R)(\mu_B+\mu_T)}\right)}{\mu_B(\mu_B + \mu_R + \mu_T)}. \tag{3.31}$$

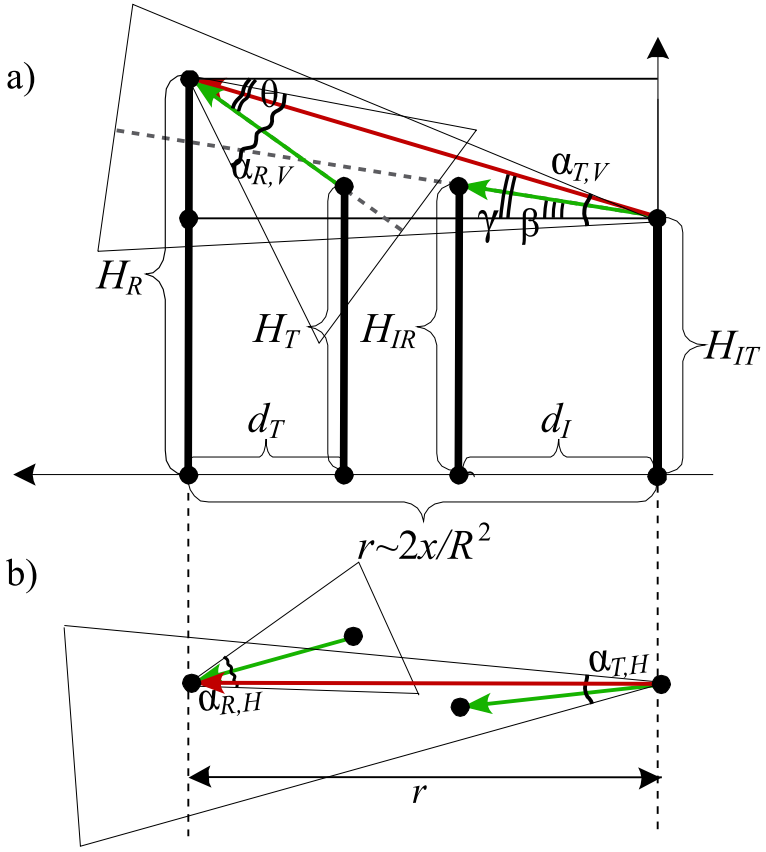

Figure 3.4. *Exposure probability for directional antennas*

Substituting (3.31) into ((3.22)) and simplifying, we arrive at (3.19). □

Fig. 3.4 illustrates the exposure. At a 2D distance r between the tagged receiver and the interference source $p_C(r)$ the probability follows

$$p_C(r) = p_V(r)p_H(r), \tag{3.32}$$

where $p_H(r)$ is the probability that interference affects the target receiver in the horizontal plane, $p_V(r)$ is the vertical exposure probability. Following [18], the probability $p_H(r)$ is found as

$$p_H(r) = \frac{\alpha_{T,H} r}{2\pi r} \frac{\alpha_{R,H} r}{2\pi r} = \frac{\alpha_{T,H}\alpha_{R,H}}{4\pi^2}, \tag{3.33}$$

where $\alpha_{T,H}$ and $\alpha_{R,H}$ are the planar directions of the antennas of the transmitters and receivers, respectively. An illustration of vertical exposure is shown in Fig. 3.4. The following statement expresses the probability $p_V(r)$.

Proposition 3. The formula

$$p_V(r) = \int_{-\infty}^{\infty} \int_{y_4-\frac{\alpha_{T,V}}{2}}^{y_4+\frac{\alpha_{T,V}}{2}} \int_{y_4-\frac{\alpha_{R,V}}{2}}^{y_4+\frac{\alpha_{R,V}}{2}} f_{\gamma,\theta,\beta}\left(y_1, y_4, y_6\right) dy_1 dy_6 dy_4, \tag{3.34}$$

where $f_{\gamma,\theta,\beta}\left(y_1, y_4, y_6\right)$ are the random angles $\{\theta, \gamma, \beta\}$ jpdf, see Fig. 3.4, and $\alpha_{T,V}$ and $\alpha_{R,V}$ are the vertical directivity of the antennas of the transmitters and receivers, respectively, determines the probability $p_V(r)$ for directional transmitters and receivers.

Proof. We consider the system $\{\theta, \gamma, \beta\}$ of RVs, see Fig. 3.4, where RV θ is the angle between the straight line from the target transmitter to the receiver and the horizon line, γ is the angle between the line from the potential interference source to the target receiver and the horizon. β is the angle between the straight line from the potential interference source to its associated receiver and horizon. Defining $\alpha_{T,V}$ and $\alpha_{R,V}$ as the vertical orientation of the transmitters and receivers, the probability of vertical antenna angles exposure is given in equation (3.34).

For the convenience, we reassign the original RV:

$$\vec{\xi} = \{\xi_1, \xi_2, \ldots, \xi_6\} = \{H_T, H_R, d_T, H_{IT}, d_I, H_{IR}\}, \tag{3.35}$$

where H_T is a height of the target transmitter and H_R is the height of a receiver, H_{IT} and H_{IR} are the heights of the transmitter-receiver interference pair, while d_T and d_I are the distances on the plane between the target and interfering pairs. In connection with the independence of the RVs jpdf ξ_1 has a multiplicative form

$$f_{\vec{\xi}}(\vec{x}) = \frac{4x_3x_5\mu_T^2\mu_R^2}{R_T^4} e^{-\mu_R x_6 - \mu_T x_4 - \mu_R x_2 - \mu_T x_1}. \tag{3.36}$$

For convenience, we also reassign the target random variables:

$$\vec{\eta}^m = \{\eta_1, \eta_4, \eta_6\} = \{\theta, \gamma, \beta\}, \tag{3.37}$$

because there are less target RVs, m, than initial RVs, n, we add the auxiliary RVs:

$$\vec{\eta} = \{\eta_1, \eta_2, \ldots, \eta_6\} = \{\theta, H_R, d_T, \gamma, d_I, \beta\}. \tag{3.38}$$

Further, the considered RV transformation and additional auxiliary functions are given by the formula

$$\begin{cases} y_1 = f_1\left(\vec{x}\right) = \theta = \tan^{-1}\left(\frac{x_1-x_2}{x_3}\right), \\ y_4 = f_4\left(\vec{x}\right) = \gamma = \tan^{-1}\left(\frac{x_4-x_2}{r}\right), \\ y_6 = f_6\left(\vec{x}\right) = \beta = \tan^{-1}\left(\frac{x_4-x_6}{x_5}\right), \end{cases} \quad \begin{cases} y_2 = f_1\left(\vec{x}\right) = x_2, \\ y_3 = f_3\left(\vec{x}\right) = x_3, \\ y_5 = f_5\left(\vec{x}\right) = x_5. \end{cases} \tag{3.39}$$

Notice that the transformation has one-to-one correspondence in the θ, γ, and $\beta = (-\pi/2, \pi/2)$ domains of interest. Therefore, inverse transformations are defined as:

$$\begin{cases} x_1 = \phi_1(\vec{y}) = y_2 + y_3 \tan y_1, \\ x_4 = \phi_4(\vec{y}) = y_2 + r \tan y_4, \\ x_6 = \phi_6(\vec{y}) = y_4 + y_5 \tan y_6, \end{cases} \quad \begin{cases} x_2 = \phi_2(\vec{y}) = y_2, \\ x_3 = \phi_3(\vec{y}) = y_3, \\ x_5 = \phi_5(\vec{y}) = y_5. \end{cases} \tag{3.40}$$

Finishing the calculation, the angles jpdf is

$$f_{\vec{\eta}}(\vec{y}) = \iiint_{\mathrm{R}^3} f_{\vec{\xi}}(\phi_1(\vec{y}^n), \ldots, \phi_n(\vec{y}^n)) |\mathbb{J}| dy_2 dy_5 dy_3, \tag{3.41}$$

where $\mathbb{J} = -r y_3 y_5 \sec^2(y_1) \sec^2(y_4) \sec^2(y_6)$ is the transformation Jacobian, and the integrand has form:

$$f_{\vec{\xi}}(\vec{\phi}^n(\vec{y}^n)) = \frac{4 y_3 y_5 \mu_R^2 \mu_T^2}{R_T^4} e^{-\mu_R(y_4 - y_5 \tan[y_6]) - \mu_T(x \tan[y_4] + y_2)} \times e^{-\mu_T(y_3 \tan[y_1] + y_2) - y_2 \mu_R}. \tag{3.42}$$

Solving the integral, we arrive at:

$$\begin{aligned} & f_{\vec{\eta}}(\vec{y}) = \\ & = \int_0^{R_T} \int_{h_1}^{R_T} \int_{h_2}^{\infty} \frac{4 r y_3^2 y_5^2 \mu_R^2 \mu_T^2 \sec {y_1}^2 \sec {y_4}^2 \sec {y_6}^2}{R_T^4} e^{-\mu_R(y_4 - y_5 \tan y_6) - \mu_T(y_2 + r \tan y_4) - y_2 \mu_R - \mu_T(y_2 + y_3 \tan y_1)} dy_2 dy_5 y_3 = \\ & = \int_0^{R_T} \int_{h_1}^{R_T} \frac{4 r y_3^2 y_5^2 \mu_R^2 \mu_T^2 \sec {y_1}^2 \sec {y_4}^2 \sec {y_6}^2}{R_T^4 (\mu_R + 2\mu_T)} e^{y_5 \mu_R \tan[y_6] - r \mu_T \tan[y_4] - y_3 \mu_T \tan[y_1] - (\mu_R + 2\mu_T) h_2 - y_4 \mu_R} dy_5 dy_3. \end{aligned} \tag{3.43}$$

where

$$\begin{aligned} h_1 &= \max\{0, -\cot(y_1) y_4, -\tan(y_4) r\}, \\ h_2 &= \max\{0, -\tan(y_1) y_3, -\tan(y_4) r\}. \end{aligned} \tag{3.44}$$

The last two integrals can also be solved, which will lead to the expression of the closed form $f_{\gamma,\theta,\beta}(y_1, y_4, y_6)$. The angles jpdf final form of the can be found online: `http://winter.rd.tut.fi/supplement.pdf`. □

Lets note, that scheme for the numerical integration (3.34) is provided in A.

Proposition 4. The covariance between the received signal power the interference is defined as:

$$E[P_R I] = A^2 \lambda \pi R_I^2 p_C E[(X_i X_0)^{-\zeta}]. \tag{3.45}$$

By integration we obtain $E[(X_0X_i)^{-\zeta}]$

$$\int_0^{R_I}\int_0^{R_T}\int_0^{\infty}\int_0^{\infty}\int_0^{\infty}\frac{[(x_1-x_2)^2+x_5^2]^{-\frac{\zeta}{2}}}{[(x_1-x_3)^2+x_4^2]^{\frac{\zeta}{2}}}f(x_1\dots x_5)dx_1\dots dx_5, \tag{3.46}$$

with associated jpdf as follows:

$$f(x_1\dots x_5)=\frac{\mu_T\mu_R^2e^{-\mu_Tx_1-\mu_R(x_2+x_3)}4x_4x_5}{(R_TR_I)^2}. \tag{3.47}$$

Proof. Writing the desired expression as $K_{P_R,I}=E[P_RI]-\mu_{P_R}\mu_I$, we get

$$E[P_RI]=E\Big[AX_0^{-\zeta}\sum_{i=1}^{N}AX_i^{-\zeta}\Big], \tag{3.48}$$

where X_0 is the distance between the target Tx and Rx, X_i, $i=1,2\dots N$ is the distance between the i-th interfering Tx and the target Rx.

Utilizing Wald's identity [74] we have

$$E[P_RI]=A^2E[N]E[(X_iX_0)^{-\zeta}], \tag{3.49}$$

where $E[N]=\lambda\pi R_I^2p_C$, $E[(X_0X_i)^{\zeta}]$ are the unknowns.

Then writing $E[(X_0X_i)^{-\zeta}]$ as

$$E[([(H_R-H_T)^2-r_0][(H_R-H_I)^2-r_i])^{-\frac{\zeta}{2}}], \tag{3.50}$$

where r_0 – is a constant and, therefore, we arrive at (3.45). □

3.2.3 Special Cases

Our proposed three-dimensional model includes several sub-models of different computational complexity. We summarize the details of these models below.

Directional transmitters omnidirectional receivers

It is expected that the mobile terminals will not have a big number of antenna elements, what implies that their antennas will have lower gains and directivity. Thus, assuming that all receivers are equipped with omnidirectional antennas, this will dramatically lower the computation time of the model results. The main alteration between the main model and the model with omni-directional receiver antennas is the consideration of exposure probability. The probability of planar exposure has the form $p_H(r)=\alpha/2\pi$, and the calculation of the probability of vertical exposure for this case is shown in the appendix B.

Communication objects with fixed heights

Some of the mmWave deploiments assume that the heights of transceivers are konown in advance and have constant value, with relaxation of the parameters simplifies the model significantly. We also can use this sub-model for approximation of the model with random heights, setting the height values to the RV means. Propositions establishing the exposure and blocking probabilities for the fixed heights are shown in Appendix B. Particularly for this model we can establish these values as a closed form expressions, which reduce the computational time dramatically.

Two-dimensional model

The main variation between the three- and two-dimensional models is the blocking probability $p_B(r)$, and the exposure probability $p_C(r)$. Accordingly, $p_C(r)$ reduces to $p_C(r) = (\alpha_T \alpha_R)/4\pi^2$, where α_T and α_R are the horizontal directions of the antennas of the transmitters and receivers. The LoS blockage zone for this case has sides $2r_B$ and D, where D is a RV with pdf $f_D(d) = 2d/R_T^2$, see Fig. 3.3. The conditional probability of blockage is determined by the probability of the absence of points in a region of spatial Poisson process (void probability) see, for example, [9]

$$p_B(r) = e^{-2\lambda r_B r}. \tag{3.51}$$

According to (3.12), the moments of interference have the form

$$E[I^n] = \int_{r_B}^{R_I} (1 - e^{-2\lambda r_B r}) \tfrac{\alpha}{(} A r^{-\zeta})^n 2\pi 2\lambda\pi r dr = A^n \alpha \lambda \Big[\tfrac{E_{n\zeta-1}\left(-2\lambda r_B^2\right)}{r_B^{\zeta n-2}} - \tfrac{E_{n\zeta-1}(-2\lambda r_B R_I)}{R_I^{\zeta n-2}} \Big], \tag{3.52}$$

where $E_n(x)$ is the exponential integral function [75].

Now, we estimate the average SIR value using second-order expansion (3.11), where $K_{P,I} = 0$ for the two-dimensional case interference moments are (3.52) and the average received signal power is

$$E[P_R] = \int_{r_B}^{R_T} A x^{-\zeta} \frac{2x}{R_T^2} dx = \frac{2A\left(r_B^{2-\zeta} - R_T^{2-\zeta}\right)}{(\zeta - 2) R_T^2}. \tag{3.53}$$

4 NUMERICAL ASSESSMENT

In this chapter, we layout the evaluation of a proposed model numerical example. First, we evaluate the developed model accuracy using simulation model. Next, we investigate the deviations of the simplified models results and propose ranges of input parameters in which they can be used for adequately close approximations. Table 4.1 system parameters used for the model accuracy assessment. Lastly, we study the performance of several deployments, examine various configurations of antenna arrays that correspond to different options in mmWave networks, along with typical examples of wireless interactions, including AP-UEs, AUV and D2D. Table 4.2 summarizes the system parameters of the wireless network used for the numerical example.

4.1 Accuracy assessment

The probability of vertical exposure, p_V, is a critical parameter that distinguishes two-dimensional and three-dimensional models from each other. Since the calculation of the probability p_V is also the most challenging stage of the calculation in the model proposed, first we estimate the efficiency of the possible approximations p_V and then continue to illustrate the accuracy of the SIR approximation.

4.2 Effects of System Parameters

In this work we made several assumptions on the system parameters in regard to height distributions, interference and noise. First we evaluate the impact of these assumptions on the results. Fig. 4.1 shows the SIR mean value for different device heights distributions and two sets of antenna parameters (see. Table 4.1), as a function of the space intensity of transmitter and receiver pairs in the PPP. Because of the fact that exponential distribution has only one parameter, for the evaluation we chose the standard deviations of all distributions to match exponential i.e. the mean squared. From the results we see that the choice of distribution does not significantly effect the results. One can notice that the Exponential distribution shows slightly higher mean SIR values on the whole range of the parameters. Further, analyzing the results we should always take this effect into account.

Previously, we made an assumption, that all the the blocked signal doesn't contribute to the aggregated interference in the tagged receiver. But for the more accurate calculations

Table 4.1. *Parameters for the model accuracy assessment.*

Parameter	**Value**
Bandwidth	1 GHz
Blockage loss (if used)	7 dB
Distributions of heights	**Exponential**; Uniform; Laplace; Gaussian
Johnson–Nyquist noise power	-84 dBm
Maximum distance between Rx and interferer	150 m
Maximum distance between Tx and Rx	15 m
Mean blocker height	1.7 m
Mean Rx height	1.5 m
Mean Tx height	5 m
Number of experiments for each point	10000
Path loss exponent	2.1
PPP intensity of communicating pairs	(0.01;0.1) pairs per m^2
Rx antenna planar directivity	25°
Rx antenna vertical directivity	25°
Standard deviations of heights	Equal to mean heights
Tx antenna planar directivity	2°;25°
Tx antenna vertical directivity	25°

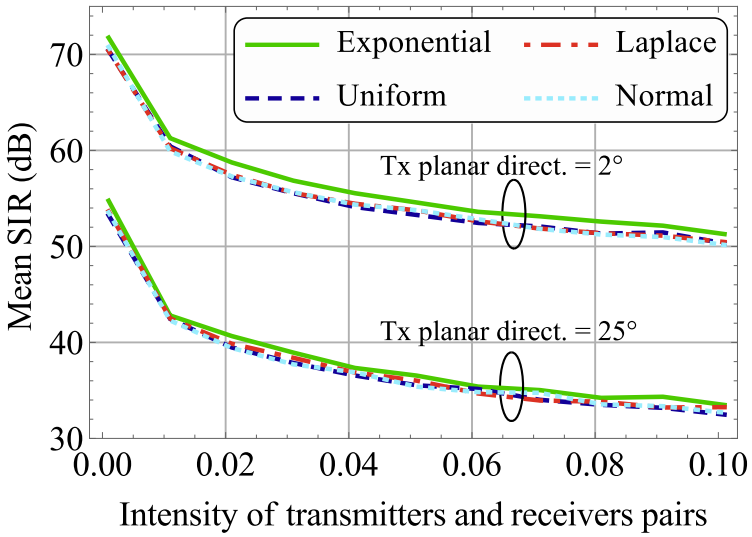

Figure 4.1. *The effect of height distribution*

we can extend the basic model, particularly the equation for the total interference to account also for the blocked interfering signal as highly attenuated one. To extend the model we modify (3.12). Now, formula for the total interference on the receiver takes the

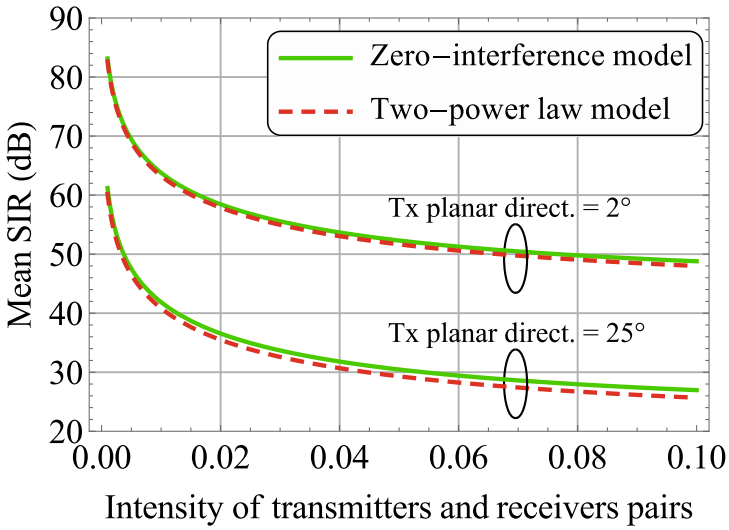

Figure 4.2. *The effect of blocked interference*

form

$$E[I^n] = \int_0^{R_I} E[I^n_{1,0}(r)]p_C(r)[1-p_B(r)]2\lambda\pi r dr + \\ + \int_0^{R_I} E[I^n_{1,1}(r)]p_C(r)p_B(r)2\lambda\pi r dr, \tag{4.1}$$

where $E[I^n_{1,0}]$ and $E[I^n_{1,1}]$ are the two separate terms taking into account the non-blocked and shadowed interference. We get the the two terms similarly to $E[I^n_1]$ in Proposition 1. Usually, this two components will be different in terms of path loss model.

Fig. 4.2 compares the two approaches when we totally ignore the blocked interference ("zero-interference model") and the more accurate approach ("two power law model"). For the second model we chose the path loss model to have additional 7dB loss if the signal was abstracted. Analyzing the results (Fig. 4.2), we notice that the two power law model slightly more pessimistic than the first one, but not drastically. Here we should note that the second approach effects the computational complexity by doubling the amount of computing time without giving much of the improvement of the results.

Lastly, Fig. 4.3 shows the comparison for SIR and SINR values. Here, we compare our basic analytical model to the one accounting for Johnson–Nyquist noise having -174 dBm/Hz of power. The bandwidth of interest is chosen to be 1GHz thus implying that the aggregate noise power is -84 dBm. For this particular example of mmWave system adding noise, as one can notice, does not introduce much of a difference to the results. In our case, the emitted power is 1W and Tx = $\{2^\circ \times 25^\circ\}$; Rx = $\{25^\circ \times 25^\circ\}$, Tx = $\{25^\circ \times 25^\circ\}$; Rx = $\{25^\circ \times 25^\circ\}$ leading to combined gains of the Tx and Rx antennas being 36 dB and 47 dB, respectively for the two considered directivities, $\{2^\circ \times 25^\circ\}$ and $\{25^\circ \times 25^\circ\}$. We would like to note that for smaller values of emitted power and higher values of antenna gains, the effect of noise could be more profound. The developed methodology allows to estimate both SIR and SINR for a wide range of systems parameters.

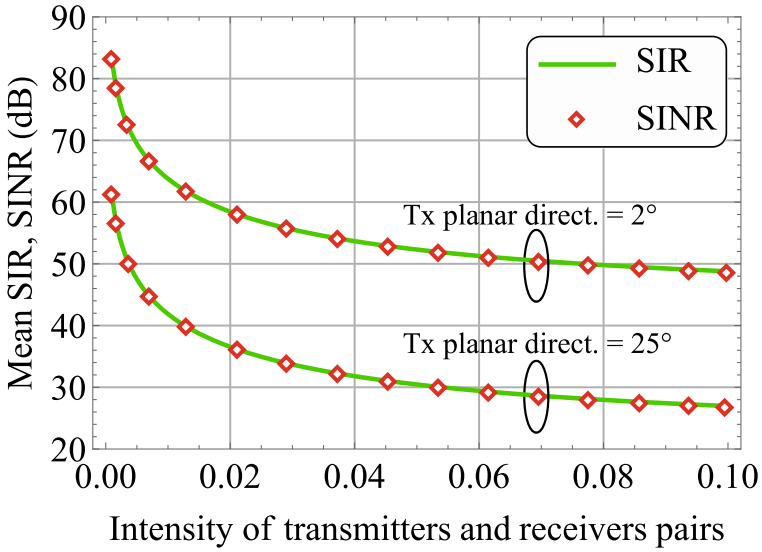

Figure 4.3. *The effect of noise*

To do this, in the beginning of Section IV we need to consider a Taylor expansion around the means of the function S=g(x,y)=P(x)/(I(y)+N), where N is the cumulative noise over the band of interest provided by BN0. Here, B is the bandwidth of interest, N0 is the Johnson-Nyquist noise at one Hertz, N0=-174dBm. Using the same approach as before the Taylor expansion takes the following form

$$E\left[\frac{P}{I+N}\right] = E\left[f(P,I)\right] \approx \frac{\mu_P}{\mu_I+N} - \frac{}{(\mu_I+N)^2} + \frac{\sigma_I^2\mu_P}{(\mu_I+N)^3}, \tag{4.2}$$

where μ_I and μ_P are the interference and received power means, σ_I^2 and σ_P^2 are the interference and received power variances, and K_{PI}^2 is the covariance.

Fig. 4.4 illustrates the vertical exposure probability p_V dependence on a distance between an interfering transmitter and the target receiver for two types of transmitter antenna vertical directionality. The graph shows both the analytical model as well as confidence intervals from the simulation of the equivalent model using the Monte Carlo method. The simulation results demonstrate that the proposed model approximates the SIR values well enough and satisfies the confidence intervals. Similar conclusions one can get from Fig. 4.5, which illustrates SIR dependence on the spatial intensity of interacting devices and the horizontal directionality of the transmitters.

4.3 System Behavior Analysis

The main proposed three-dimensional framework needs a lot of computational resources, this is mainly explained by the calculation of the probability of vertical exposure. Therefore, for the practical usage, we need less complex framework that can offer a suitable level of accuracy. In this section, we define the input system parameters range where simplified models are suitable for evaluation purposes. Additionally to a simple two-

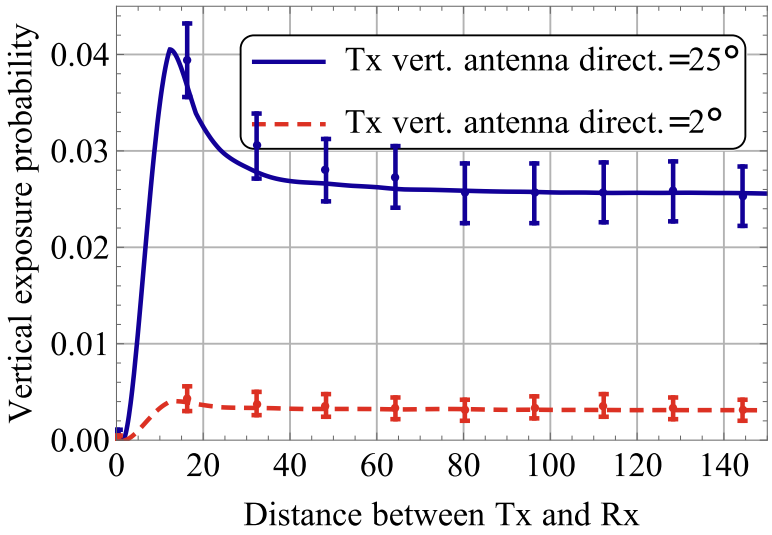

Figure 4.4. *Vertical exposure probability*

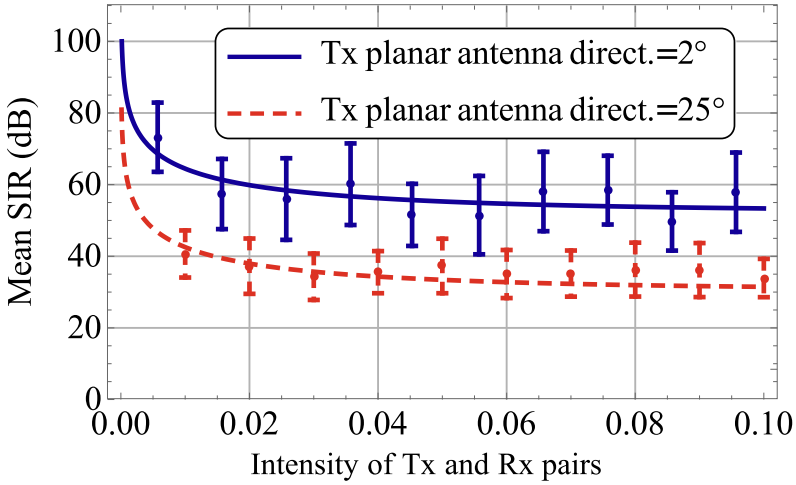

Figure 4.5. *Values of SIR*

dimensional model that does account for heights randomness and probability of vertical exposure, we further propose various combined models with fixed / random heights (FH / RH) that use or do not use the probability of vertical exposure probability ($\pm$PV). We designate these components as PV, FH, and RH. Therefore, our three-dimensional model is will be labeled as (RH $+$ PV).

Fig. 4.9-4.11 show the mean SIR values for different models depending on two system parameters: the spatial intensity of the communicating pairs of devices, λ, and the vertical orientation of the transmitter antennas, $\alpha_{T,V}$. Fig. 4.9 shows that no simpler models provide a precise mean SIR approximation over the entire λ range. Interestingly, a two-dimensional model that does not any how takes into account the third dimension dramatically overestimates system SIR characteristics. The reason is that neglecting the heights of communication objects sharply increases the likelihood of blocking the LoS, which ultimately leads to less interference received at the target receiver. Three other models,

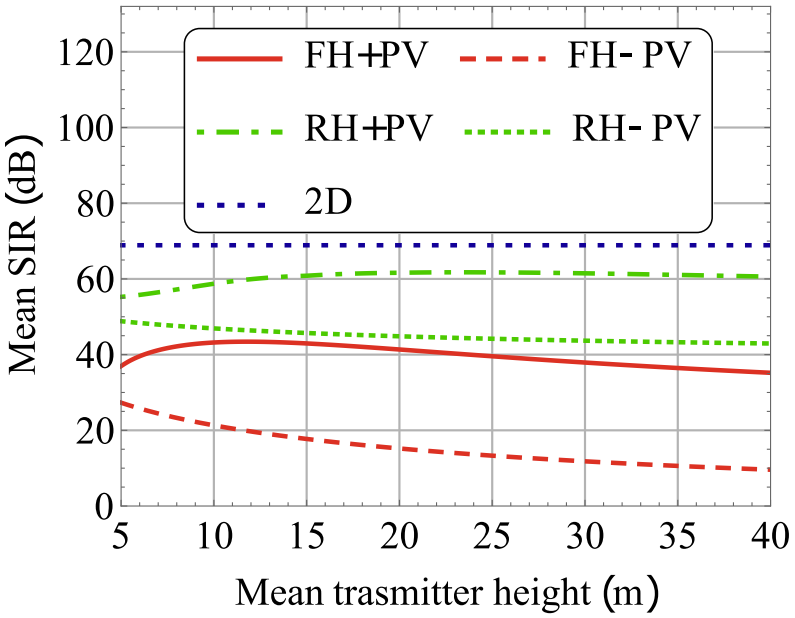

Figure 4.6. *Varying mean Tx height*

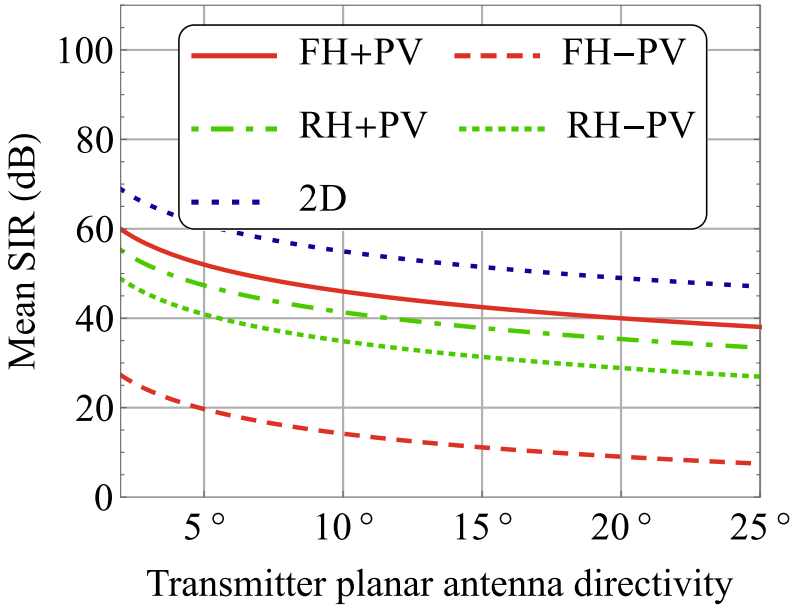

Figure 4.7. *Varying* $\alpha_{T,H}$, $\alpha_{T,V} = 2°$

which partly take into account the effects of the third dimension, underestimate the actual performance in terms of SIR. A model that takes into account the randomness of heights, but ignores the probability of vertical exposure, remains closest to the proposed three-dimensional model in an acceptable range of intensities of communicating pairs. The difference between these models is not more than a few decibels and decreases with decreasing λ. The least accurate model is a model with fixed heights and not taking into account the probability of vertical exposure.

Next, we consider the effect of the vertical direction of the antennas, as shown in Fig. 4.10 and Fig. 4.11 or two values of the horizontal directivity of the transmitter antennas, $\alpha_{T,H} =$

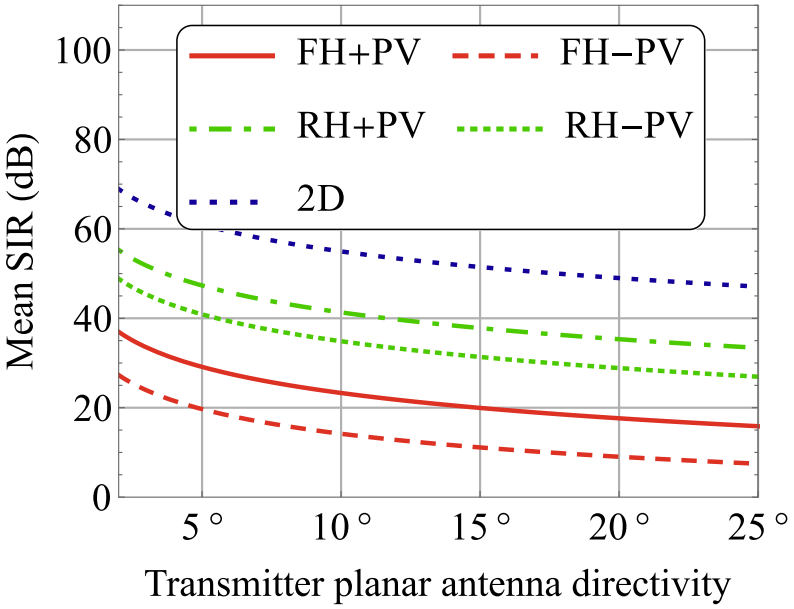

Figure 4.8. *Varying* $\alpha_{T,H}$, $\alpha_{T,V} = 25°$

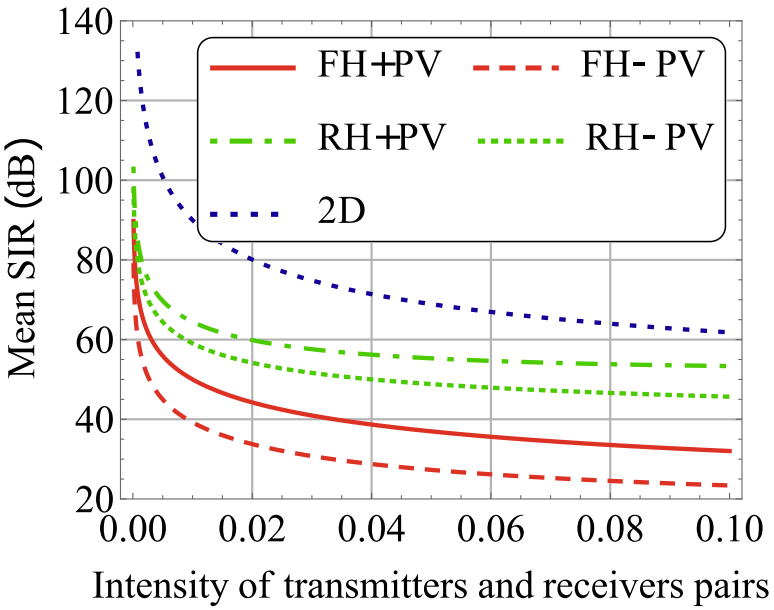

Figure 4.9. *Varying pairs spatial intensity*

$2°$ and $\alpha_{T,H} = 25°$. Obviously, the SIR values predicted by three models that do not take into account vertical exposure are independent of $\alpha_{T,V}$. For other models, a higher vertical directivity of the antennas leads to an increase in system performance for the considered horizontal directivity values. At the same time, the model with fixed heights gives a significant deviation from the actual average SIR values for all considered values of the vertical directivity of the antennas. In particular, it is at least 10 dB for two horizontal directivity values. For small values of the vertical directivity of the antennas in the range $(1° - 5°)$, a model that does not take into account the probability of vertical exposure provides an adequate approximation, as we already noted, analyzing Fig. 4.9. his conclusion remains valid as long as the directivity of the receiver antennas is quite large, that

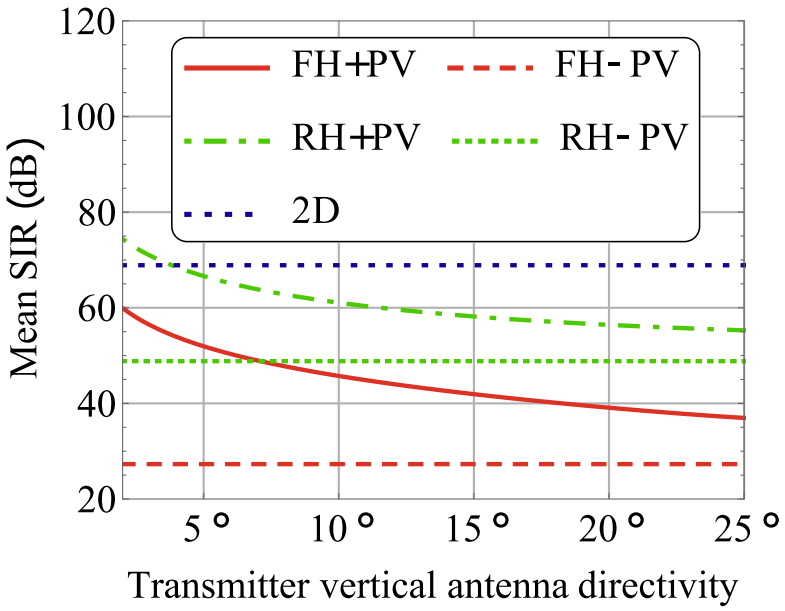

Figure 4.10. *Varying* $\alpha_{T,V}$, $\alpha_{T,H} = 2°$

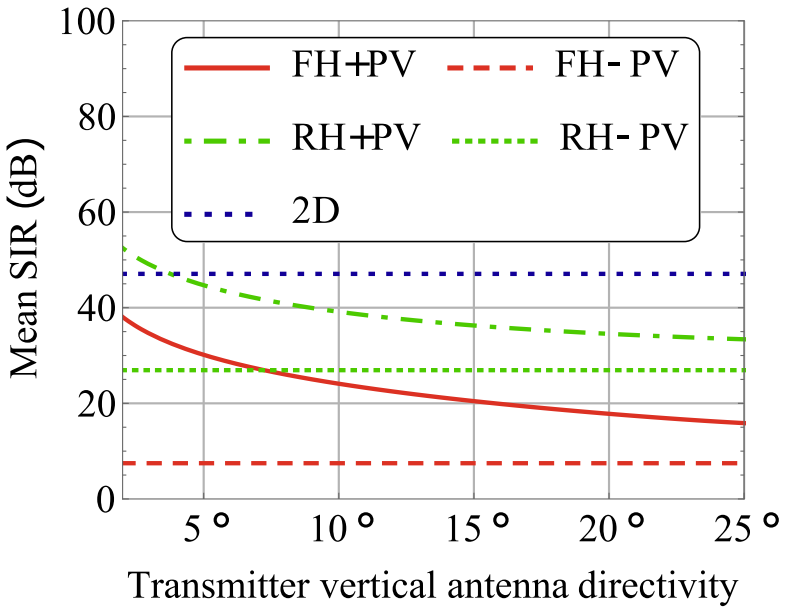

Figure 4.11. *Varying* $\alpha_{T,V}$, $\alpha_{T,H} = 25°$

is, 20° or more. Other models are too pessimistic regarding system performance.

The average heights of the transmitters and receivers are critical system parameters that affect the likelihood of vertical exposure p_V , and therefore SIR values. Fig. 4.6 shows the effect of average transmitter heights on mean SIR. The average height of the transmitters affects the SIR performance only on a rather small subset of values, that is, in the range of 1-10 meters, which implies that this parameter is important for AP-UE communication scenarios. For other models, the average SIR value remains constant. When analyzing the approximations, one can note that only a model with fixed heights, which also takes into account the probability of vertical impact (FH + PV), captures the actual trend in the

average SIR. However, quantitatively, these two curves are approximately 20 dB apart. For average transmitter heights, the random-height model, which neglects the p_V effect, provides an accurate approximation, while for large average transmitter heights, the results for the simplest two-dimensional model are relatively close. Note that the influence of the average height of the receivers is qualitatively similar and therefore omitted.

We continue to consider the effect of the horizontal directivity of the transmitter antennas, as shown in Fig. 4.7 and Fig. 4.8 for the vertical orientations of the transmitter antennas 2° and 25°, espectively. Intuitively, the higher the horizontal directionality of the transmitter antennas, the higher the system performance. Also, a monotonous trend is visible for the considered vertical directionality values. The actual SIR values predicted by our model are between two models offering approximations over the entire range of presented typical scenarios. Two-dimensional, taking into account the 2° vertical directionality of the transmitters (with random heights and excluding vertical exposure and with fixed heights taking into account vertical exposure probability). However, with large values of the vertical directivity, only the latter remains sufficiently accurate.

Finally, we note that a flat two-dimensional model offers an optimistic upper bound for the estimation of the SIR value over the entire range of input parameters of the system. On the other hand, a model with fixed heights that do not take into account the vertical exposure probability always shows lower estimates of SIR values. The difference between these models can reach 60 dB, which means that none of them can be used as a boundary estimate of network performance. The smallest computationally complex model that offers a reasonable approximation is a model with a fixed height and vertical orientation. However, for specific ranges of input parameters, its prediction may also deviate by more than 10 dB from the actual mean SIR values.

4.4 Typical Scenarios

By design, our developed model can characterize various types of communication scenarios. Now we begin to assess the SIR performance for three typical communication scenarios: (a) AP-UE, (b) UAV-UE, and (c) D2D. Table 4.2 contains the script parameters, except for the heights of the communicating objects. The average heights of the transmitters and receivers for the corresponding three cases are $(5, 1.5)$, $(40, 1.5)$, and $(1.5, 1.5)$, respectively.

The use of highly directional antennas at both ends of the radio link leads to difficulties associated with the need to create efficient and accurate electronic beamforming mechanisms [76, 77]. It is especially critical when the transmitters and receivers are mobile devices. For these scenarios, we consider three different directivity options at both ends of the wireless link. The first scenario suggests the use of 128×4 and 4×4 antenna arrays on transmitters and receivers, respectively, and corresponds to modeling devices of the first mmWave systems generation. The second and third cases using $128 \times 128/4 \times 4$ and $128 \times 128/64 \times 64$ antenna arrays (transmitter/receiver) reflect mmWave systems of the

Table 4.2. *Values of the modeled parameters.*

Parameter	Value
Average height of a blocker, $E[H_B] = 1/\mu_B$	1.7 m
Blocker's body radius, r_B	0.3 m
Carrier frequency, f_c	28 GHz
Maximum distance between tagged pair of devices, R_T	15 m
Mean receiver height, $E[H_R] = 1/\mu_R$	1.5 m
Mean transmitter height, $E[H_T] = 1/\mu_T$	5 m
Path loss exponent, ζ	2.1
Planar Rx antenna directivities, $\alpha_{R,H}$	25°
Planar Tx antenna directivities, $\alpha_{T,H}$	25°
Radius of an area around the tagged Rx, from where interference can be received, R_I	150 m
Spatial density of Rx nodes, λ	0.05 1/m^2
Vertical Rx antenna directivities, $\alpha_{R,V}$	25°
Vertical Tx antenna directivities, $\alpha_{T,V}$	2°

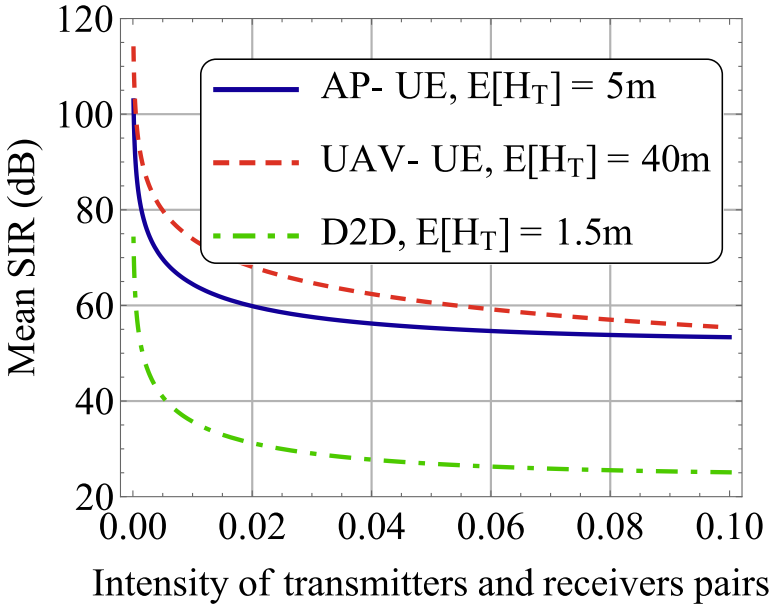

Figure 4.12. *Now, Tx:*128×4*, Rx:*4×4

next generations. We call these three cases *Now*, *Near Future*, and *Distant Future*.

Fig. 4.12-4.14 show the average SIR value depending on the intensity of the interacting pairs for various transmitter and receiver antenna configurations, as well as different communication scenarios. By analyzing the setting of the antenna arrays, the benefits achieved by using the more advanced antenna design of the transmitters and receivers are mainly quantitative, that is, at the same intensity of the interacting pairs, using more antenna elements improves SIR. Significantly, a notable improvement is associated with an increase in the vertical direction of the transmitters during the transition from 128×4

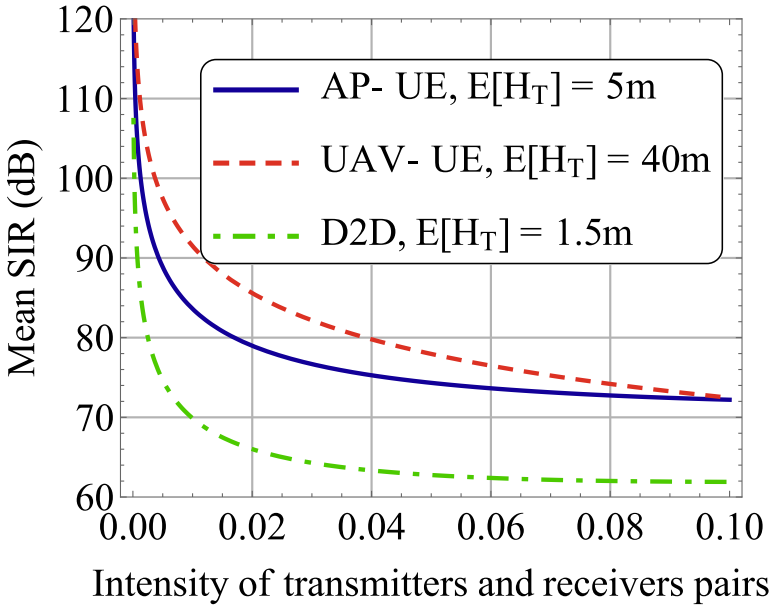

Figure 4.13. *Near future, Tx:*128×128*, Rx:*4×4

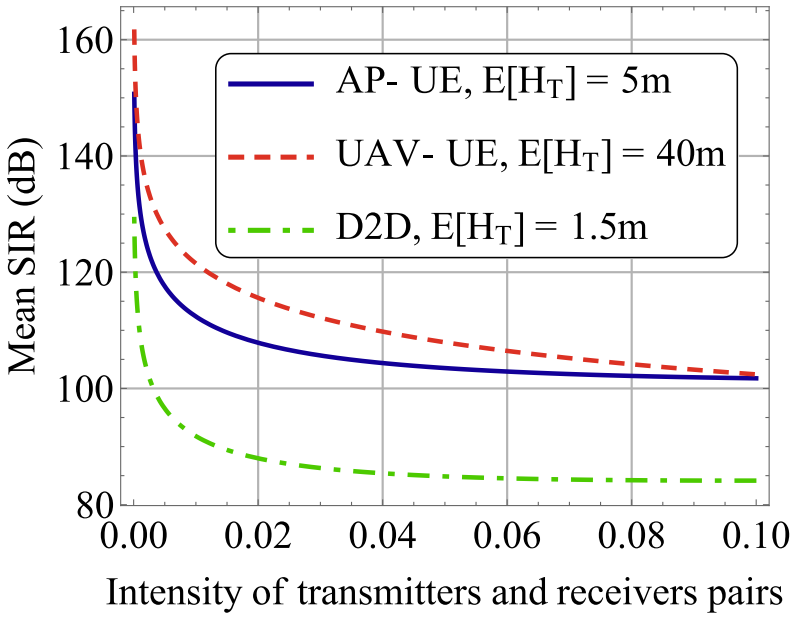

Figure 4.14. *Distant future, Tx:*128×128*, Rx:*64×64

to 128×128. Analyzing the data for the same antenna configurations, one can note that worse SIR values characterize the D2D scenario. This behavior is a direct consequence of the lower average height of the transmitters, which maximizes the likelihood of vertical exposure. The UAV scenario achieves the best performance for all antenna configurations. However, the difference in values at transmitter heights from 5 to 40 meters is insignificant for high spatial intensities of interacting pairs and increases with decreasing parameter λ.

5 CONCLUSION

In this work, we developed a three-dimensional stochastic geometry model for estimating SINR in 5G networks operating in mmWave frequency range, the features of wireless systems operating in the millimeter frequency range, such as the directivity of antennas, the effect of signal blockages by human bodies, and random heights of communication entities. The developed framework is suitable for analyzing several types of wireless networks, including standard models based on APs, systems with drones, and D2D communication using mmWave. The most accurate model, which takes into account all the mmWave systems features cannot be simplified to the closed-form or tabular functions, but still can be used for numerical solutions. To get more practical tools for evaluating SINR values, we also introduced several simplified models that relaxed some of the assumptions. We showed the parameter ranges and scenarios at which these sub-models can be utilized.

Using the basic model, we analyzed the importance of accounting for the randomness of the communicating device heights and exposure probability to evaluate the characteristics of three-dimensional mmWave models accurately. Conventional two-dimensional models of stochastic geometry always provide overly optimistic results that can overestimate the average SIR values of up to 20 dB. On the other hand, a fixed-height model that ignores the vertical exposure is too pessimistic for evaluating some of the scenarios. The presented results for a simplified model can deviate for up to 40-60 dB, which makes them useful only as lower limits for the network planning. The third sub-model, which accounts for vertical exposure probability but not for the randomness of the transceivers heights, can be used as a much less computationally expensive tool but fairly accurate one for the broad range of the scenarios.

Lastly, we compared the typical mmWave deployment types: Access point, Drone, and Device-to-device based scenarios. We showed that with the same parameters UAV-based scenario showed the highest performance potential due to the ability to avoid the inter-cell interference utilizing high antenna directivities with the advantage of higher altitudes. On the other hand, D2D-based deployment showed the worst results in terms of SIR due to the opposite reasons.

REFERENCES

[1] R. Kovalchukov, A. Samuylov, D. Moltchanov, A. Ometov, S. Andreev, Y. Koucheryavy and K. Samouylov. Modeling three-dimensional interference and SIR in highly directional mmWave communications. *2017 IEEE Global Communications Conference (GLOBECOM)*. IEEE. 2017, 1–7.

[2] R. Kovalchukov, D. Moltchanov, A. Samuylov, A. Ometov, S. Andreev, Y. Koucheryavy and K. Samouylov. Analyzing effects of directionality and random heights in drone-based mmWave communication. *IEEE Transactions on Vehicular Technology* 67.10 (2018), 10064–10069.

[3] R. Kovalchukov, D. Moltchanov, A. Samuylov, A. Ometov, S. Andreev, Y. Koucheryavy and K. Samouylov. Evaluating SIR in 3D Millimeter-Wave Deployments: Direct Modeling and Feasible Approximations. *IEEE Transactions on Wireless Communications* 18.2 (2018), 879–896.

[4] Cisco. *Global Mobile Data Traffic Forecast 2016–2021*. White Paper. 2017.

[5] G. George and A. Lozano. Impact of reflections in enclosed mmWave wearable networks. *Proc. of 6th International Workshop on Computational Advances in Multi-Sensor Adaptive Processing (CAMSAP)*. IEEE. 2015, 201–204.

[6] K. Venugopal and R. W. Heath. Location based performance model for indoor mmWave wearable communication. *Proc. of International Conference on Communications (ICC)*. IEEE. 2016, 1–6.

[7] Y. Wang and Z. Shi. Millimeter-Wave Mobile Communications. *5G Mobile Communications*. Springer, 2017, 117–134.

[8] J. G. Andrews, S. Buzzi, W. Choi, S. V. Hanly, A. Lozano, A. C. Soong and J. C. Zhang. What will 5G be?: *IEEE Journal on Selected Areas in Communications* 32.6 (2014), 1065–1082.

[9] M. Gapeyenko, A. Samuylov, M. Gerasimenko, D. Moltchanov, S. Singh, E. Aryafar, S.-p. Yeh, N. Himayat, S. Andreev and Y. Koucheryavy. Analysis of human-body blockage in urban millimeter-wave cellular communications. *Proc. of International Conference on Communications (ICC)*. IEEE. 2016, 1–7.

[10] A. Orsino, A. Ometov, G. Fodor, D. Moltchanov, L. Militano, S. Andreev, O. N. Yilmaz, T. Tirronen, J. Torsner, G. Araniti et al. Effects of Heterogeneous Mobility on D2D-and Drone-Assisted Mission-Critical MTC in 5G. *IEEE Communications Magazine* 55.2 (2017), 79–87.

[11] Y. Orlov, E. Kirina-Lilinskaya, A. Samuylov, A. Ometov, D. Moltchanov, Y. Gaimamaka, S. Andreev and K. Samouylov. Time-Dependent SIR Analysis in Shopping Malls Using Fractal-Based Mobility Models. *Proc. of International Conference on Wired/Wireless Internet Communication*. Springer. 2017, 16–25.

[12] S. N. Chiu, D. Stoyan, W. S. Kendall and J. Mecke. *Stochastic geometry and its applications*. John Wiley & Sons, 2013.

[13] F. Bacelli and B. Blaszczyszyn. *Stochastic Geometry and Wireless Networks, Part I: Theory*. Now Publishers, 2009.

[14] A. Kammoun, M. Debbah, M.-S. Alouini et al. 3D massive MIMO systems: Modeling and performance analysis. *IEEE Transactions on Wireless Communications* 14.12 (2015), 6926–6939.

[15] A. K. Gupta, X. Zhang and J. G. Andrews. SINR and throughput scaling in ultra-dense urban cellular networks. *IEEE Wireless Communications Letters* 4.6 (2015), 605–608.

[16] J.-M. Kelif and M. Coupechoux. A 3D Spatial Fluid Model for Wireless Networks. *arXiv preprint arXiv:1604.04457* (2016).

[17] V. Petrov, D. Moltchanov and Y. Koucheryavy. On the Efficiency of Spatial Channel Reuse in Ultra-Dense THz networks. *Proc. IEEE Globecom*. Dec. 2015.

[18] V. Petrov, M. Komarov, D. Moltchanov, J. M. Jornet and Y. Koucheryavy. Interference and SINR in Millimeter Wave and Terahertz Communication Systems With Blocking and Directional Antennas. *IEEE Transactions on Wireless Communications* 16.3 (2017), 1791–1808.

[19] M. Di Renzo. Stochastic geometry modeling and analysis of multi-tier millimeter wave cellular networks. *IEEE Transactions on Wireless Communications* 14.9 (2015), 5038–5057.

[20] K. Venugopal and R. Heath. Millimeter Wave Networked Wearables in Dense Indoor Environments. *IEEE Access* 4 (Apr. 2016), 1205–1221.

[21] S. Singh, M. N. Kulkarni, A. Ghosh and J. G. Andrews. Tractable model for rate in self-backhauled millimeter wave cellular networks. *IEEE Journal on Selected Areas in Communications* 33.10 (2015), 2196–2211.

[22] D. Moltchanov, P. Kustarev and Y. Koucheryavy. Analytical approximations for interference and SIR densities in terahertz systems with atmospheric absorption, directional antennas and blocking. *Physical Communication* 26 (2018), 21–30.

[23] J. Nasreddine, J. Riihijärvi, A. Achtzehn and P. Mähönen. The World is not flat: Wireless communications in 3D environments. *Proc. of 14th International Symposium and Workshops on a World of Wireless, Mobile and Multimedia Networks (WoWMoM)*. IEEE. 2013, 1–9.

[24] F. Letourneux, Y. Corre, E. Suteau and Y. Lostanlen. 3D coverage analysis of LTE urban heterogeneous networks with dense femtocell deployments. *Journal on Wireless Communications and Networking* 2012.1 (2012), 319.

[25] A. Müller, J. Hoydis, R. Couillet et al. Optimal 3D cell planning: A random matrix approach. *Proc. of Global Communications Conference (GLOBECOM)*. IEEE. 2012, 4512–4517.

[26] D. Soldani and A. Manzalini. Horizon 2020 and beyond: On the 5G operating system for a true digital society. *IEEE Vehicular Technology Magazine* 10.1 (2015), 32–42.

[27] GSM Associattion. www.gsma.com. July 2019.

[28] ITU. *Setting the Scene for 5G: Opportunities and Challenges*. Technical Report. Nov. 2018.

[29] S. E. Elayoubi, M. Fallgren, P. Spapis, G. Zimmermann, D. Martín-Sacristán, C. Yang, S. Jeux, P. Agyapong, L. Campoy, Y. Qi et al. 5G service requirements and operational use cases: Analysis and METIS II vision. *2016 European Conference on Networks and Communications (EuCNC)*. IEEE. 2016, 158–162.

[30] ITU-T. *Requirements of IMT-2020 fixed mobile convergence*. Rec. ITU-R Y.3110. Jan. 2018.

[31] ITU-R. *IMT Vision: Framework and overall objectives of the future development of IMT for 2020 and beyond*. Rec. ITU-R M.2083. July 2015.

[32] F. Boccardi, R. W. Heath Jr, A. Lozano, T. L. Marzetta and P. Popovski. Five disruptive technology directions for 5G. *arXiv preprint arXiv:1312.0229* (2013).

[33] E. Dahlman, G. Mildh, S. Parkvall, J. Peisa, J. Sachs, Y. Selén and J. Sköld. 5G wireless access: requirements and realization. *IEEE Communications Magazine* 52.12 (2014), 42–47.

[34] S. A. Busari, S. Mumtaz, S. Al-Rubaye and J. Rodriguez. 5G millimeter-wave mobile broadband: Performance and challenges. *IEEE Communications Magazine* 56.6 (2018), 137–143.

[35] R. K. Saha, S. Nanba, K. Nishimura, Y.-b. Kim and K. Yamazaki. RAN Architectural Evolution Framework toward 5G and Beyond Cellular-An Overview. *2018 IEEE 29th Annual International Symposium on Personal, Indoor and Mobile Radio Communications (PIMRC)*. IEEE. 2018, 592–593.

[36] Z. Pi, J. Choi and R. Heath. Millimeter-wave gigabit broadband evolution toward 5G: Fixed access and backhaul. *IEEE Communications Magazine* 54.4 (2016), 138–144.

[37] O. Abari, H. Hassanieh, M. Rodriguez and D. Katabi. Millimeter wave communications: From point-to-point links to agile network connections. *Proceedings of the 15th ACM Workshop on Hot Topics in Networks*. ACM. 2016, 169–175.

[38] T. Hößler, M. Simsek and G. P. Fettweis. Mission reliability for URLLC in wireless networks. *IEEE Communications Letters* 22.11 (2018), 2350–2353.

[39] H. Cao, S. Gangakhedkar, A. R. Ali, M. Gharba and J. Eichinger. A testbed for experimenting 5G-V2X requiring ultra reliability and low-latency. *WSA 2017; 21th International ITG Workshop on Smart Antennas*. VDE. 2017, 1–4.

[40] Z. Li, M. A. Uusitalo, H. Shariatmadari and B. Singh. 5g urllc: Design challenges and system concepts. *2018 15th International Symposium on Wireless Communication Systems (ISWCS)*. IEEE. 2018, 1–6.

[41] J. Sachs, G. Wikstrom, T. Dudda, R. Baldemair and K. Kittichokechai. 5G radio network design for ultra-reliable low-latency communication. *IEEE Network* 32.2 (2018), 24–31.

[42] D. Soldani, Y. J. Guo, B. Barani, P. Mogensen, I. Chih-Lin and S. K. Das. 5G for ultra-reliable low-latency communications. *Ieee Network* 32.2 (2018), 6–7.

[43] C. Bockelmann, N. Pratas, H. Nikopour, K. Au, T. Svensson, C. Stefanovic, P. Popovski and A. Dekorsy. Massive machine-type communications in 5G: Physical and MAC-layer solutions. *IEEE Communications Magazine* 54.9 (2016), 59–65.

[44] N. H. Mahmood, M. Lauridsen, G. Berardinelli, D. Catania and P. Mogensen. Radio resource management techniques for eMBB and mMTC services in 5G dense small cell scenarios. *2016 IEEE 84th Vehicular Technology Conference (VTC-Fall)*. IEEE. 2016, 1–5.

[45] C. Bockelmann, N. K. Pratas, G. Wunder, S. Saur, M. Navarro, D. Gregoratti, G. Vivier, E. De Carvalho, Y. Ji, Č. Stefanović et al. Towards massive connectivity support for scalable mMTC communications in 5G networks. *IEEE access* 6 (2018), 28969–28992.

[46] *AT&T Makes World's First eCPRI Call for Millimeter Wave*. Sept. 2019. URL: https://about.att.com/innovationblog/2019/09/first_ecpri_call_for_millimeter_wave.html.

[47] A. Ometov, D. Moltchanov, M. Komarov, S. V. Volvenko and Y. Koucheryavy. Packet Level Performance Assessment of mmWave Backhauling Technology for 3GPP NR Systems. *IEEE Access* 7 (2019), 9860–9871.

[48] T. S. Rappaport et al. *Wireless communications: principles and practice*. Vol. 2. prentice hall PTR New Jersey, 1996.

[49] B. D. Steinberg. Principles of aperture and array system design: Including random and adaptive arrays. *New York, Wiley-Interscience, 1976. 374 p.* (1976).

[50] W. Roh, J. Y. Seol, J. Park, B. Lee, J. Lee, Y. Kim, J. Cho, K. Cheun and F. Aryanfar. Millimeter-wave beamforming as an enabling technology for 5G cellular communications: theoretical feasibility and prototype. *IEEE Communications Magazine* 52.2 (Feb. 2014), 106–113.

[51] W. Hong, K.-H. Baek, Y. Lee, Y. Kim and S.-T. Ko. Study and prototyping of practically large-scale mmWave antenna systems for 5G cellular devices. *IEEE Communications Magazine* 52.9 (2014), 63–69.

[52] P. Nayeri, M. Liang, R. A. Sabory-Garcı, M. Tuo, F. Yang, M. Gehm, H. Xin, A. Z. Elsherbeni et al. 3D printed dielectric reflectarrays: low-cost high-gain antennas at sub-millimeter waves. *IEEE Transactions on Antennas and Propagation* 62.4 (2014), 2000–2008.

[53] G. Brooker, R. Hennessey, C. Lobsey, M. Bishop and E. Widzyk-Capehart. Seeing through dust and water vapor: Millimeter wave radar sensors for mining applications. *Journal of Field Robotics* 24.7 (2007), 527–557.

[54] S. Sun, G. R. MacCartney and T. S. Rappaport. A novel millimeter-wave channel simulator and applications for 5G wireless communications. *Proc. of International Conference on Communications (ICC)*. IEEE. 2017, 1–7.

[55] A. Ghosh, T. A. Thomas, M. C. Cudak, R. Ratasuk, P. Moorut, F. W. Vook, T. S. Rappaport, G. R. MacCartney, S. Sun and S. Nie. Millimeter-wave enhanced local area systems: A high-data-rate approach for future wireless networks. *IEEE Journal on Selected Areas in Communications* 32.6 (2014), 1152–1163.

[56] F. Khan and Z. Pi. mmWave mobile broadband (MMB): Unleashing the 3–300GHz spectrum. *Proc. of 34th Sarnoff Symposium*. IEEE. 2011, 1–6.

[57] T. L. Frey. The Effects of the Atmosphere and Weather on the Performance of a mm-Wave Communication Link. *Applied Microwave and Wireless* 11 (1999), 76–81.

[58] H. J. Liebe, T. Manabe and G. A. Hufford. Millimeter-wave attenuation and delay rates due to fog/cloud conditions. *IEEE Transactions on Antennas and Propagation* 37.12 (1989), 1617–1612.

[59] A. Foessel, S. Chheda and D. Apostolopoulos. Short-range millimeter-wave radar perception in a polar environment. (1999).

[60] A. Y. Nashashibi, K. Sarabandi, S. Oveisgharan, M. C. Dobson, W. S. Walker and E. Burke. Millimeter-wave measurements of foliage attenuation and ground reflectivity of tree stands at nadir incidence. *IEEE Transactions on Antennas and Propagation* 52.5 (2004), 1211–1222.

[61] F. K. Schwering, E. J. Violette and R. H. Espeland. Millimeter-wave propagation in vegetation: Experiments and theory. *IEEE Transactions on Geoscience and Remote Sensing* 26.3 (1988), 355–367.

[62] E. K. Smith. Centimeter and millimeter wave attenuation and brightness temperature due to atmospheric oxygen and water vapor. *Radio Science* 17.06 (1982), 1455–1464.

[63] H. J. Liebe and D. H. Layton. Millimeter-wave properties of the atmosphere: Laboratory studies and propagation modeling. *NASA STI/Recon Technical Report N* 88 (1987).

[64] E. E. Reber, R. L. Mitchell and C. J. Carter. *OXYGEN ABSORPTION IN THE EARTH'S ATMOSPHERE.* Tech. rep. AEROSPACE CORP EL SEGUNDO CALIF LAB OPERATIONS, 1968.

[65] G. R. MacCartney and T. S. Rappaport. 73 GHz millimeter wave propagation measurements for outdoor urban mobile and backhaul communications in New York City. *ICC*. 2014, 4862–4867.

[66] H. Zhao, R. Mayzus, S. Sun, M. Samimi, J. K. Schulz, Y. Azar, K. Wang, G. N. Wong, F. Gutierrez Jr and T. S. Rappaport. 28 GHz millimeter wave cellular communication measurements for reflection and penetration loss in and around buildings in New York city. *ICC*. 2013, 5163–5167.

[67] C. Slezak, V. Semkin, S. Andreev, Y. Koucheryavy and S. Rangan. Empirical effects of dynamic human-body blockage in 60 ghz communications. *IEEE Communications Magazine* 56.12 (2018), 60–66.

[68] G. R. MacCartney, T. S. Rappaport and S. Rangan. Rapid fading due to human blockage in pedestrian crowds at 5G millimeter-wave frequencies. *GLOBECOM 2017-2017 IEEE Global Communications Conference*. IEEE. 2017, 1–7.

[69] M. Gapeyenko, A. Samuylov, M. Gerasimenko, D. Moltchanov, S. Singh, M. R. Akdeniz, E. Aryafar, N. Himayat, S. Andreev and Y. Koucheryavy. On the temporal

effects of mobile blockers in urban millimeter-wave cellular scenarios. *IEEE Transactions on Vehicular Technology* 66.11 (2017), 10124–10138.

[70] 3GPP. *Study on channel model for frequencies from 0.5 to 100 GHz (Release 14)*. 3GPP TR 38.901 V14.1.1. July 2017.

[71] S. Singh, R. Mudumbai and U. Madhow. Interference Analysis for Highly Directional 60-GHz Mesh Networks: The Case for Rethinking Medium Access Control. *IEEE/ACM Transactions on Networking* 19.5 (Oct. 2011), 1513–1527.

[72] M. Petrera and Y. B. Suris. Spherical geometry and integrable systems. *Geometriae Dedicata* 169.1 (Apr. 2014), 83–98. ISSN: 1572-9168. DOI: 10.1007/s10711-013-9843-4. URL: https://doi.org/10.1007/s10711-013-9843-4.

[73] M. G. Kendall et al. *The Advanced Theory of Statistics*. Vol. 1, Ed. 4. Charles Griffin and Co., Ltd., 42 Drury Lane, London, 1948.

[74] S. Ross. *Introduction to probability models*. Academic Press, 2010.

[75] M. Abramowitz and I. Stegun. *Handbook of Mathematical Functions with Formulas, Graphs, and Mathematical Tables*. Dover, 1965.

[76] V. Va, J. Choi and R. W. Heath. The impact of beamwidth on temporal channel variation in vehicular channels and its implications. *IEEE Transactions on Vehicular Technology* 66.6 (2016), 5014–5029.

[77] S. Hur, T. Kim, D. J. Love, J. V. Krogmeier, T. A. Thomas, A. Ghosh et al. Millimeter Wave Beamforming for Wireless Backhaul and Access in Small Cell Networks. *IEEE Trans. Communications* 61.10 (2013), 4391–4403.

A EVALUATING VERTICAL EXPOSURE PROBABILITY

Fig. A.1 demonstrates $f_{\gamma,\theta,\beta}\,(y_1, y_4, y_6)$, the jpdf of the angles $\{\gamma, \theta, \beta\}$. Fig. A.2 shows the regions where $|\theta-\gamma| < \alpha_{T,V}/2 \cap |\theta-\beta| < \alpha_{R,V}/2$. To assess the probability of vertical exposure we need to integrate $f_{\gamma,\theta,\beta}$ over this region in accordance with (3.34). Lastly, Fig. A.3 shows the intersections of the integration regions and the piecewise integrand domnains.

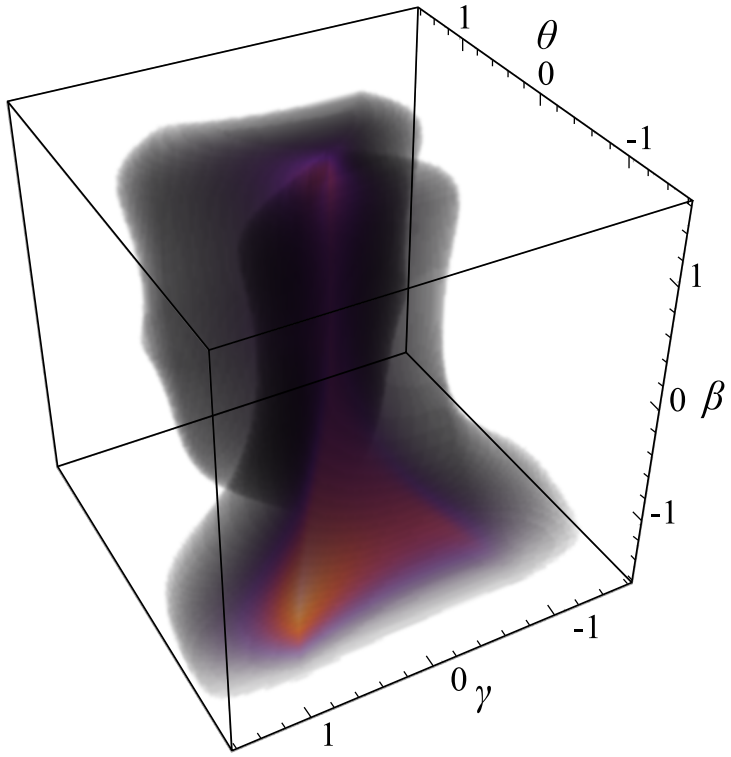

Figure A.1. *$\{\gamma, \theta, \beta\}$ jpdf*

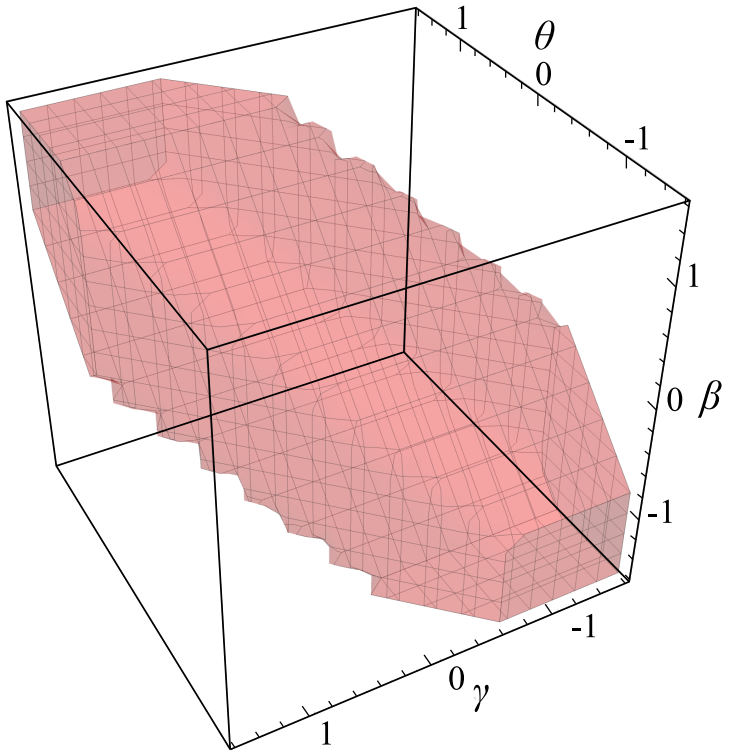

Figure A.2. *Region of integration*

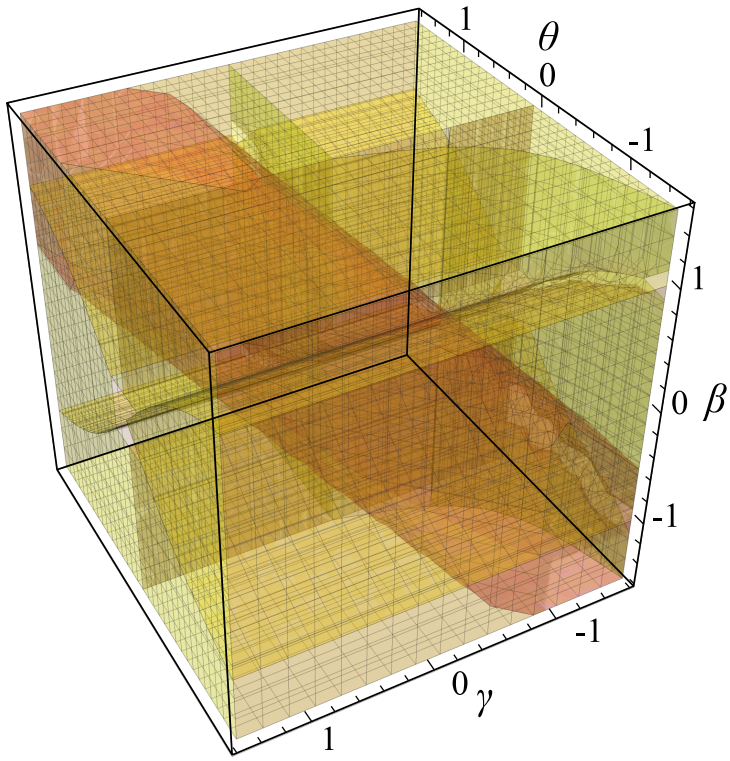

Figure A.3. $\{\gamma, \theta, \beta\}$ *jpdf piecewise domains intersecting region of integration*

B ADDITIONAL PROPOSITIONS FOR THE SPECIAL CASES OF THE MODEL

In this appendix, we provide the propositions for special model cases: (1) vertical exposure probability for the case there receiver nodes have omnidirectional antenna patterns, (2) probability of vertical exposure, and (3) the blockage likelihood for the fixed heights of transmitter and receiver nodes case .

Proposition 5. The probability of vertical exposure $p_V(r)$ for a directional antenna of transmitters and omnidirectional at the receivers is established by integrating angles β, θ jpdf over $|\beta-\theta| < \alpha_{T,V}/2$ (Fig. B.1), i.e.

$$p_V(r) = \int_{-\frac{\pi}{2}}^{\frac{\pi}{2}} \int_{y_4-\frac{\alpha_{T,V}}{2}}^{y_4+\frac{\alpha_{T,V}}{2}} f_{\beta,\theta}\left(y_1, y_4\right) dy_1 dy_4, \tag{B.1}$$

where $f_{\beta,\theta}\left(y_1, y_4\right)$ is jpdf β and θ has the form

$$f_{\eta_1,\eta_4}\left(y_1, y_4\right) = \iiint\limits_{\mathrm{R}^3} f_{\vec{\xi}^n}\left[\phi_i(\vec{y}^n)\right] |\mathbb{J}| dy_2 dy_3 dy_5 = \int\limits_0^{R_I} \int\limits_0^{R_T} \int\limits_{l(y_i)}^{\infty} \frac{4\mu^3 y_3^2 y_5^2 \mathrm{e}^{-\mu(y_3 \tan(y_1)+3y_2+y_5 \tan(y_4))}}{\sec^{-2}(y_1)\sec^{-2}(y_4) R_I^2 R_T^2} dy_2 dy_3 dy_5 =$$
$$= \int\limits_0^{R_I} \int\limits_0^{R_T} \frac{4\mu^2 y_3^2 y_5^2 e^{-\mu(3l(y_i)+y_3 \tan(y_1)+y_5 \tan(y_4))}}{\sec^{-2}(y_1)\sec^{-2}(y_4) 3R_I^2 R_T^2} dy_3 dy_5 = \int\limits_0^{R_I} f_{\eta_1\eta_4\eta_5}(y_1, y_4, y_5) dy_5. \tag{B.2}$$

Proof. Let $\vec{\xi}^n = \{\xi_1, \ldots, \xi_4\} = \{H_R, H_T, d_T, H_{IT}\}$ and note that due to the independence of the components involved its jpdf has a multiplicative form

$$f_{\vec{\xi}^n}(\vec{x}^n) = \frac{2x_3}{R_T^2} \mu_R e^{-\mu_R x_1} \mu_T e^{-\mu_T x_2} \mu_T e^{-\mu_T x_4}. \tag{B.3}$$

Let also $\vec{\eta}^m = \{\eta_1, \eta_4\} = \{\beta, \theta\}$. We supplement the target RVs with auxiliary once since the number of target RVs, m, is less than the number of input RVs, n,

$$\vec{\eta}^n = \{\eta_1, \ldots, \eta_4\} = \{\beta, H_T, d_T, \theta\}. \tag{B.4}$$

Therefore, the transformation in question takes form

$$\begin{cases} y_1 = f_1(\vec{x}^n) = \beta = \arctan[(x_1 - x_2)/x_3] \\ y_4 = f_4(\vec{x}^n) = \theta = \arctan[(x_4 - x_2)/r] \end{cases}, \tag{B.5}$$

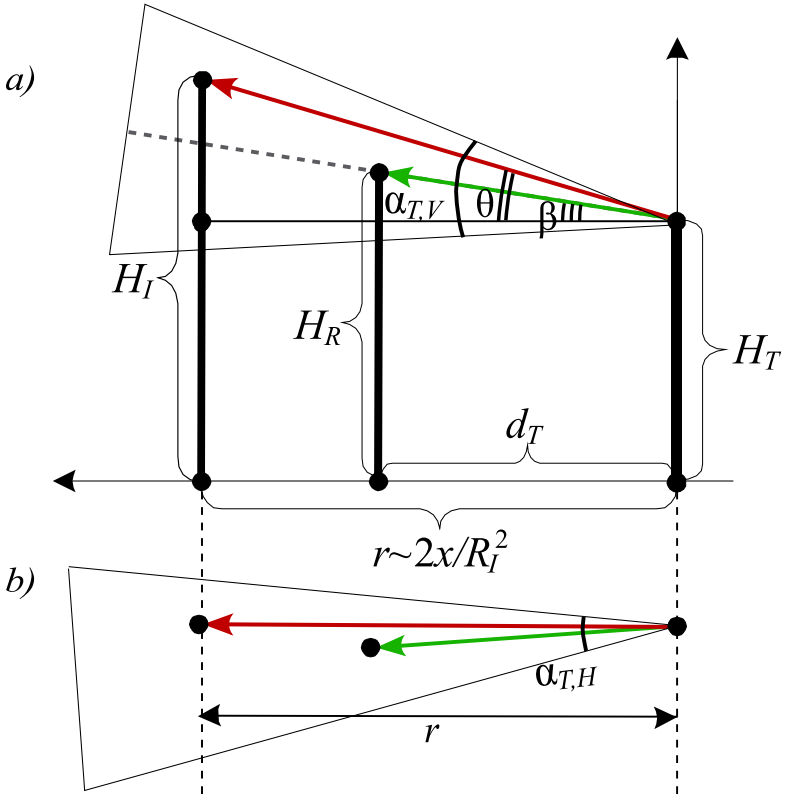

Figure B.1. *Vertical exposure for non-directional receivers*

and auxiliary functions – $f_i(\vec{x}^n) = x_i$, $i = \{2, 3\}$.

Inverse functions have one-to-one correspondence in the values domain, i.e.

$$\begin{cases} x_1 = \phi_1(\vec{y}^n) = y_2 + y_3 \tan y_1 \\ x_4 = \phi_4(\vec{y}^n) = y_2 + r \tan y_4 \end{cases}, \tag{B.6}$$

which are complemented with $x_i = \phi_i(\vec{y}^n) = y_i$, $i = \{2, 3\}$.

Further, we represent jpdf as

$$f_{\vec{\eta}^n}(\vec{y}^n) = f_{\xi^n}(\phi_1(\vec{y}^n), \ldots, \phi_n(\vec{y}^n))|\mathbb{J}|, \tag{B.7}$$

where the Jacobian transform is calculated as $\mathbb{J} = y_3 r \sec^2 y_1 \sec^2 y_4$ and jpdf $f_{\vec{\xi}^n}(\phi_1(\vec{y}^n), \ldots, \phi_n(\vec{y}^n))$ takes form (B.3).

Denoting $l(y_i) = \max(0, -y_3 \tan y_1, -r \tan y_4)$, we get (B.2). Performing the last integra-

tion, we come to the jpdf β and θ, $f_{\beta,\theta}(y_1, y_4) =$

$$\begin{cases} \frac{-4r\cot(y_1)\csc^2(y_1)\sec^2(y_4)[1-e^{R_T\mu\tan(y_1)}+2R_T\mu\tan(y_1)+RT^2\mu^2\tan^2(y_1)]}{3R_T^2\mu e^{\mu[R_T\tan(y_1)+r\tan[y_4]]}}, & y_1 \geq 0 \cap y_4 \geq 0, \\ \frac{4r\cot(y_1)\csc^2(y_1)\sec^2(y_4)[e^{R_T\mu\tan(y_1)}-2R_T\mu\tan(y_1)-R_T^2\mu^2\tan^2(y_1)-1]}{3RT^2\mu e^{R_T\mu\tan(y_1)+2r\mu\tan(y_4)}}, & \\ & y_4 < 0 \cap (R_T\tan y_1 \geq r\tan y_4 \cup y_1 \geq 0), \\ \frac{2e^{2R_T\mu\tan(y_1)}RT^2\mu^2-2e^{2R_T\mu\tan(y_1)}R_T\mu\cot(y_1)-\cot^2(y_1)+e^{2R_T\mu\tan(y_1)}\cot^2(y_1)}{6r^{-1}\csc^{-1}(y_1)\sec^{-1}(y_1)\sec^{-12}(y_4)R_T^2\mu e^{r\mu\tan(y_4)}}, & y_1 < 0 \cap y_4 \geq 0, \\ \frac{r\cot(y_1)\csc(y_1)\sec^2(y_4)}{6R_T^2\mu e^{r\mu\tan(y_4)}} \times & \\ \Big(e^{2R_T\mu\tan(y_1)}\csc(y_1) - 9e^{2r\mu\tan(y_4)}\csc(y_1) + 8e^{3r\mu\tan(y_4)}\csc(y_1) - & \\ -2e^{2R_T\mu\tan(y_1)}R_T\mu\sec(y_1) + 2e^{2R_T\mu\tan(y_1)}R_T^2\mu^2\sec(y_1)\tan(y_1) - & \text{elsewhere.} \\ -6e^{2r\mu\tan(y_4)}r\mu\csc(y_1)\tan(y_4) - 6e^{2r\mu\tan(y_4)}r^2\mu^2\csc(y_1)\tan^2(y_4)\Big), & \end{cases} \tag{B.8}$$

□

Proposition 6. The vertical exposure probability for fixed transmitter and receiver heights, h_T and h_R, is given by the formula

$$p_V(r) = p_V(r, \alpha_{T,V})p_V(r, \alpha_{R,V}), \tag{B.9}$$

where the probability $p_V(r, \alpha)$ is equal to

$$\begin{cases} \frac{(h_T-h_R)^2\left[\cot\left(\frac{\alpha}{2}-\gamma\right)^2-\cot\left(\frac{\alpha}{2}+\gamma\right)^2\right]}{R_T^2}, & (h_T - h_R)r \in U_1, \\ \frac{1-(h_T-h_R)^2\cot\left(\frac{\alpha}{2}+\gamma\right)^2}{R_T^2}, & (h_T - h_R)r \in U_2, \end{cases} \tag{B.10}$$

where domains are defined as

$$U_1 = (A_+, B) \cup (B, A_+),\ U_2 = (A_+, A_-) \cup (A_-, B), \tag{B.11}$$

and $A_\pm = \cot(\pm\alpha/2 + \gamma_0)$, $B = \cot([\pi - \alpha]/2)$.

Proof. Note that when the heights of the nodes of the transmitters and receivers are constant, the angles θ, γ, and β are mutually independent, see Fig. B.1. Thus, the probability of vertical impact $p_V(r)$ can be written as $p_V(r) = p_V(r, \alpha_{T,V})p_V(r, \alpha_{R,V})$ is the likelihood that the transmitter "hits" the non-target receiver and the antenna of the receiver is oriented towards the interfering transmitter, respectively. These probabilities can be established as follows.

Let ξ be the distance between the transmitter and receiver, and α be the directivity of the antenna. Denoting the desired angle by ϵ, we have

$$p_V(r, \alpha) = \int_{\gamma-\alpha/2}^{\gamma+\alpha/2} f_\epsilon(x)dx, \tag{B.12}$$

where $f_\epsilon(x)$ is pdf of RV ϵ.

Transformation of interest is $\phi(y) = (h_T - h_R)\cot(y)$ and pdf is $f_\xi(x) = 2R_T^{-2}x$. Finishing the shown transformation, we obtain $f_\epsilon(y)$ as follows

$$f_\epsilon(y) = \frac{2(h_T - h_R)^2 \cot(y)\csc(y^2)}{R_T^2},\ 0 < y < \frac{\pi}{2}. \tag{B.13}$$

Solving the integral, we arrive at (B.10). □

Proposition 7. The probability of blocking in the Poisson field of blockers with fixed heights of transmitters and receivers, h_T and h_R, is

$$p_B(r) = 1 - e^{\frac{2\lambda\left(e^{-h_R\mu_B} - e^{-h_T\mu_B}\right)r_B r}{(h_R - h_T)\mu_B}}. \tag{B.14}$$

Proof. Assuming $h_T > h_R$, note that the height of the LoS path is evenly distributed within (h_R, h_T). Since the pdf of the differences between the LoS and the blocker height are uniformly distributed over $(0, R_I)$, G_r is a convolution of uniform and exponential distributions, i.e.

$$\begin{aligned} f_{G_r}(y) = \frac{e^{-(h_R + h_T - y)\mu_B}\left(e^{h_R\mu_B} - e^{h_T\mu_B}\right)}{h_R - h_T} - \\ - \frac{-1 + e^{(-h_T + y)\mu_B}}{h_T - h_R},\ h_R < y \cap h_T > y. \end{aligned} \tag{B.15}$$

Then the probability of blocking by one obstacle

$$\begin{aligned} p_{B,1}(r) = 1 - Pr\{G_r > 0\} = 1 - \int_0^\infty f_{G_r}(y)dy = \\ 1 - \frac{e^{-h_R\mu_B} - e^{-h_T\mu_B} + h_R\mu_B - h_T\mu_B}{h_R\mu_B - h_T\mu_B} = \\ = \frac{-e^{-h_R\mu_B} + e^{-h_T\mu_B}}{(h_R - h_T)\,\mu_B}. \end{aligned} \tag{B.16}$$

Substituting (B.16) into (3.22), we come to (B.14). □